ACS APPLIED MATERIALS & INTERFACES

www.acsami.org

Research Article

Evaluating UiO-66 Metal–Organic Framework Nanoparticles as Acid-Sensitive Carriers for Pulmonary Drug Delivery Applications

Bader M. Jarai,[§] Zachary Stillman,[§] Lucas Attia, Gerald E. Decker, Eric D. Bloch, and Catherine A. Fromen*

Cite This: *ACS Appl. Mater. Interfaces* 2020, 12, 38989–39004

Read Online

ACCESS | Metrics & More | Article Recommendations | Supporting Information

ABSTRACT: Developing novel drug carriers for pulmonary delivery is necessary to achieve higher efficacy and consistency for treating pulmonary diseases while limiting off-target side effects that occur from alternative routes of administration. Metal–organic frameworks (MOFs) have recently emerged as a class of materials with characteristics well-suited for pulmonary drug delivery, with chemical tunability, high surface area, and pore size, which will allow for efficient loading of therapeutic cargo and deep lung penetration. UiO-66, a zirconium and terephthalic acid-based MOF, has displayed notable chemical and physical stability and potential biocompatibility; however, its feasibility for use as a pulmonary drug delivery vehicle has yet to be examined. Here, we evaluate the use of UiO-66 nanoparticles (NPs) as novel pulmonary drug delivery vehicles and assess the role of missing linker defects in their utility for this application. We determined that missing linker defects result in differences in NP aerodynamics but have minimal effects on the loading of model and therapeutic cargo, cargo release, biocompatibility, or biodistribution. This is a critical result, as it indicates the robust consistency of UiO-66, a critical feature for pulmonary drug delivery, which is plagued by inconsistent dosage because of variable properties. Not only that, but UiO-66 NPs also demonstrate pH-dependent stability, with resistance to degradation in extracellular conditions and breakdown in intracellular environments. Furthermore, the carriers exhibit high biocompatibility and low cytotoxicity in vitro and are well-tolerated in *in vivo* murine evaluations of orotracheally administered NPs. Following pulmonary delivery, UiO-66 NPs remain localized to the lungs before clearance over the course of seven days. Our results demonstrate the feasibility of using UiO-66 NPs as a novel platform for pulmonary drug delivery through their tunable NP properties, which allow for controlled aerodynamics and internalization-dependent cargo release while displaying remarkable pulmonary biocompatibility.

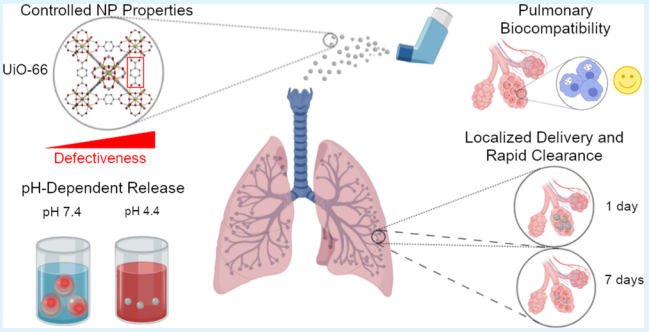

KEYWORDS: *metal–organic frameworks, UiO-66, nanoparticles, pulmonary drug delivery, defectiveness, aerosols*

INTRODUCTION

Metal–organic frameworks (MOFs) serve as a versatile class of hybrid materials composed of metal-based clusters connected in three dimensions by organic linkers. Their wide variety of possible metal clusters and organic linkers gives rise to a range of properties, allowing them to be used for applications ranging from catalysis to gas storage.[1−3] Some properties of MOFs that make them ideal candidates for these applications, such as their high surface area and pore volume, have led to more recent exploration of their use in drug delivery applications. In addition to their high loading capacity for cargo, the ability to select building units of desired hydrophilicity and to postsynthetically modify organic linkers for stealth, targeting, or biocompatibility suggests that MOFs have tailorable properties that are well-suited for many drug delivery applications.[4−6]

A key question for the use of MOFs in biological applications is their biocompatibility, as the introduction of a cytotoxic or inflammatory agent as the carrier may outweigh potential benefits. This question has arisen in particular because of the presence of metal cations in the frameworks as well as the inclusion of acidic linkers that have been shown to be cytotoxic in other applications.[7,8] As previously noted by Wuttke *et al.* among others, the biocompatibility of MOFs is highly dependent on both the MOF in question and the cells and tissues with which they will be interacting.[9,10] Accordingly, the question of toxicity must be addressed prior to the use of MOFs in a particular system. UiO-66, a zirconium-based MOF with terephthalic acid ligands, has previously been shown to be

Received: June 15, 2020
Accepted: August 6, 2020
Published: August 6, 2020

both biocompatible and water-stable, making it a good candidate for drug delivery applications.[11,12] UiO-66 also has the property of having measurable defectiveness, a property indicating that UiO-66 has linkers missing from its typical structure. This property may affect the adsorption capacity and release character of the MOFs, which may affect its potential as a drug delivery vehicle.[13] Because of these advantageous properties, UiO-66 has previously been utilized for a number of drug delivery applications, which include oral, dermal, and intravenous delivery.[14,15] Despite the wide range of delivery methods previously used for UiO-66 and other MOFs, there have been almost no instances of MOFs being formulated for pulmonary delivery.[16−18]

In general, direct pulmonary delivery *via* aerosol inhalation for the treatment of lung diseases leads to improved targeting, rapid absorption, increased local drug concentration, greater ability to interact with mucosal immune cells, and minimized off-target effects.[16,17,19] These benefits are particularly important in light of the significant global health burden of pulmonary diseases, with chronic obstructive pulmonary disorder (COPD) and lower respiratory tract infections alone leading to over 6 million annual deaths globally.[20] Not only that, but the emergent SARS-CoV-2 respiratory pathogen, which causes the COVID-19 disease pathology, highlights the need for respiratory-specific treatment approaches.[21] Design of these therapeutics is critical to effective treatment, as the delivery of particles with aerodynamic sizes of 1−5 μm results in deep lung penetration and deposition in the alveoli, an important region of the lung to target for high delivery efficiency of small molecules and proteins.[22] However, pervasive issues of polydispersity and inconsistent loading of therapeutics into delivery vehicles within pulmonary formulations, combined with confounding interpatient anatomical and breathing variables, have created challenges for consistent dosage using this route of administration. The highly tailorable properties of MOFs (pore size, cargo loading, geometric size, *etc.*) make this class of materials a unique potential carrier to address these pervasive issues encountered in pulmonary delivery.[23] Additionally, the porous nature of MOFs makes them candidates for deep lung penetration, while being geometrically small enough for cellular uptake and targeted drug delivery.[24]

Here, we examine the use of UiO-66 nanoparticles (NPs) as a novel pulmonary drug delivery vehicle. Utilizing our previously developed design rules for the fabrication of UiO-66 NPs of desired size and defectiveness, we synthesize UiO-66 NPs of constant geometric diameter with tunable defectiveness to evaluate the role of missing linkers on cargo loading of dexamethasone (dex) and rhodamine B (RhB), cargo release profiles, as well as aerodynamic behavior.[25] We show that UiO-66 NPs have high biocompatibility and low cytotoxicity both *in vitro* and *in vivo* in relevant pulmonary studies. Compared to traditional nonporous vehicles for pulmonary delivery, our results indicate that the low bulk density and tunable defectiveness of UiO-66 allows for a unique opportunity to control lung penetration and particle deposition with potential applications in inhaled immunotherapies, nanovaccines, and drug delivery. Through this comprehensive assessment of the use of UiO-66 for pulmonary drug delivery, we demonstrate the feasibility of UiO-66 NPs as a novel aerosol platform with potential delivery applications for a wide range of respiratory diseases, including COPD, lung cancers, and COVID-19.[26,27]

RESULTS AND DISCUSSION

UiO-66 NP Sizing and Defectiveness. Utilizing previously developed design rules for the variation of UiO-66 NP size and defectiveness, we synthesized a suite of particles varying in defectiveness from 1 to 15% as determined by thermogravimetric analysis (TGA) (Figures S1−S4) with a constant geometric diameter of ∼100 nm.[25] The conditions used (Table 1) yielded particles of 1, 8, 12, and 15% defectiveness, as they will be referred moving forward. Each set of NPs has diameters of ∼100 nm (Table 1) as determined *via* scanning electron microscopy (SEM) image analysis (Figure 1). The NPs were all spherical with the exception of the 1%

Table 1. UiO-66 NP Sample Sizes and Defectiveness[a]

NP sample name	TGA defectiveness (%)	geometric diameter (nm)
1% defective	1.36 ± 0.73	91.9 ± 21.0
8% defective	7.63 ± 0.46	106.5 ± 11.9
12% defective	11.84 ± 0.48	112.0 ± 13.5
15% defective	14.72 ± 0.95	110.9 ± 13.7

[a]List of samples used for biocompatibility, loading/release, and biodistribution studies along with their defectiveness as determined *via* TGA and their geometric size as determined *via* SEM. Each measurement provided is given as the average along with the standard deviation associated with three independently synthesized and measured samples.

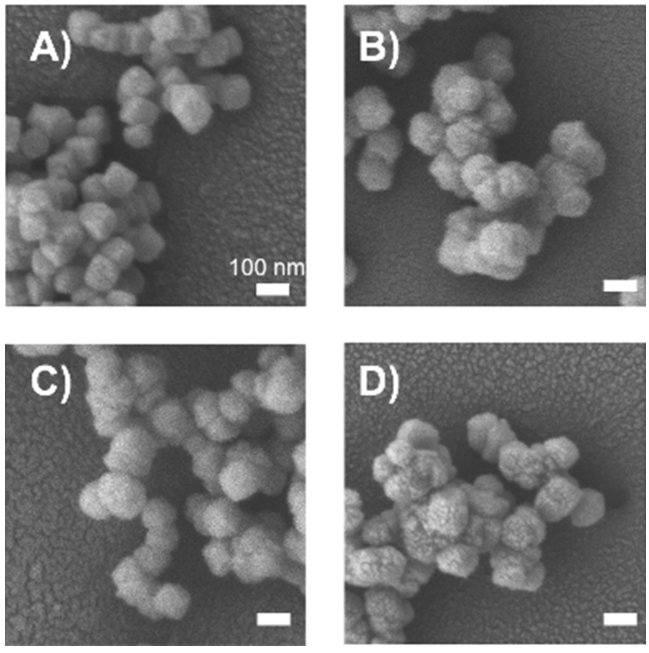

Figure 1. SEM images of UiO-66 NPs. Representative SEM images of the (A) 1% defective, (B) 8% defective, (C) 12% defective, and (D) 15% defective UiO-66 NPs. The scale bars in all images are 100 nm.

UiO-66 NPs, which have a mixed morphology with spherical and cuboidal shapes. The size and charge (measured to be −15 to −25 mV, which agrees with previous reports of UiO-66 zeta potential[28]) of the UiO-66 NPs are also in an advantageous range for phagocytic uptake, an advantage for drug delivery to alveolar macrophages, a potential therapeutic target.[29] The UiO-66 NPs will be expected to diffuse at moderate rates through mucus, which may be encountered for UiO-66 NPs

https://dx.doi.org/10.1021/acsami.0c10900
ACS Appl. Mater. Interfaces 2020, 12, 38989−39004

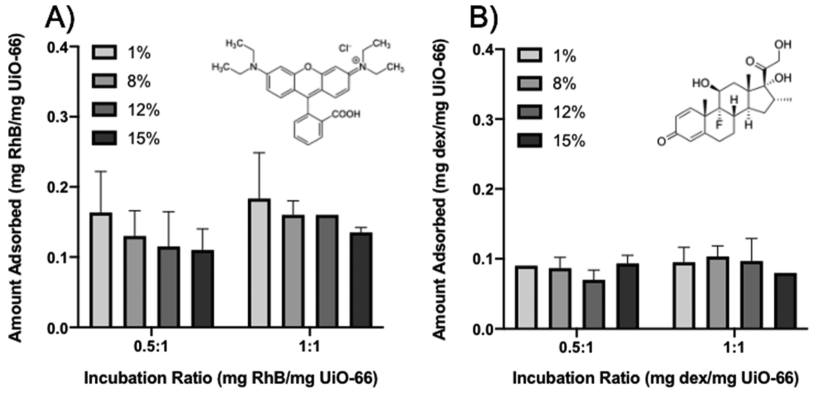

Figure 2. Loading of RhB and dex into UiO-66 NPs. Loading amounts of (A) RhB and (B) dex cargo for 1, 8, 12, and 15% defective UiO-66 NP samples at varied incubation ratios. Bars represent the mean, and error bars represent standard deviation (n = 3).

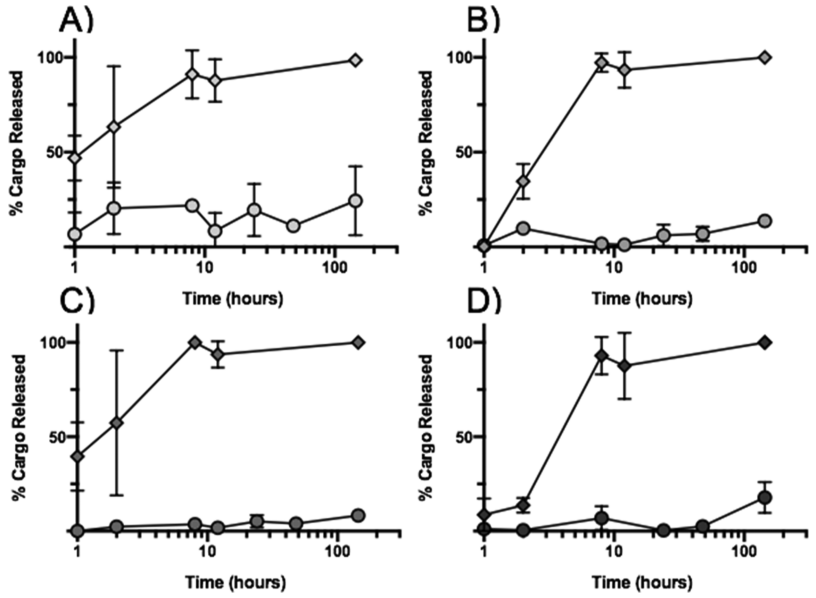

Figure 3. RhB cargo release from UiO-66 NPs. Percentage of cargo release of RhB from (A) 1% defective, (B) 8% defective, (C) 12% defective, and (D) 15% defective UiO-66 NPs over the course of 6 days (144 h). The diamond symbols are for samples incubated in ALF and the circles are for those incubated in PBS. Points represent the mean, and error bars represent standard deviation (n = 3).

that deposit in upper airways and bronchioles,[22] as charge may slow their diffusion despite their small size, which is advantageous for mucosal penetration.[30] These particle characteristics were evaluated from three independent syntheses of the respective NPs, confirming the reproducibility of the synthetic conditions used to yield the desired properties. Furthermore, the conditions identified are in line with our previous established guidelines to tune size and defectiveness a priori, enabling our evaluation of the effect of defectiveness on parameters such as biocompatibility, loading, and aerodynamic sizing independent of geometric particle size.[25]

UiO-66 Loading and Release of Model Cargo. Following size characterization, UiO-66 NPs were loaded with model cargo, RhB, and a corticosteroid, dex, to determine the extent of equilibrium cargo loading as a function of percent defectiveness. Dex is an especially relevant pulmonary therapeutic, with anti-inflammatory properties that has shown efficacy in asthma,[31] nonsmall cell lung cancer,[26] and, recently, COVID-19.[27] UiO-66 NPs of varying defectiveness were incubated with varied relative amounts of RhB or dex by mass (referred to as the incubation ratio). The amount adsorbed was determined as the mass of RhB or dex loaded per mass of UiO-66 (Figure 2). Our results demonstrate that the equilibrium loading of both RhB and dex in UiO-66 NPs is not significantly affected by either the incubation ratio or the defectiveness of the UiO-66 NPs. This is reflected *via* statistical analysis of the respective levels of loading *via* ANOVA, which reveals that there is no significant difference between the amount adsorbed per mass of UiO-66 as a function of defectiveness for either cargo. This result confirms that the removal of a potential barrier to loading (in the form of missing linkers) does not have an appreciable effect on the equilibrium loading of cargo into the UiO-66 NPs. Although the loading of dex is lower than that of RhB in UiO-66, when compared to one another, the differences in loading between RhB and dex are not statistically significant *via* Sidak's multiple comparisons, although the categorical factor was determined to be significant *via* ANOVA. We hypothesize that the lower amount of dex adsorbed may be related to the decreased capacity for pi−pi stacking relative to RhB, which has far greater number of pi bonds. This indicates that the structure and size of cargo are likely both important factors to determine

https://dx.doi.org/10.1021/acsami.0c10900
ACS Appl. Mater. Interfaces 2020, 12, 38989−39004

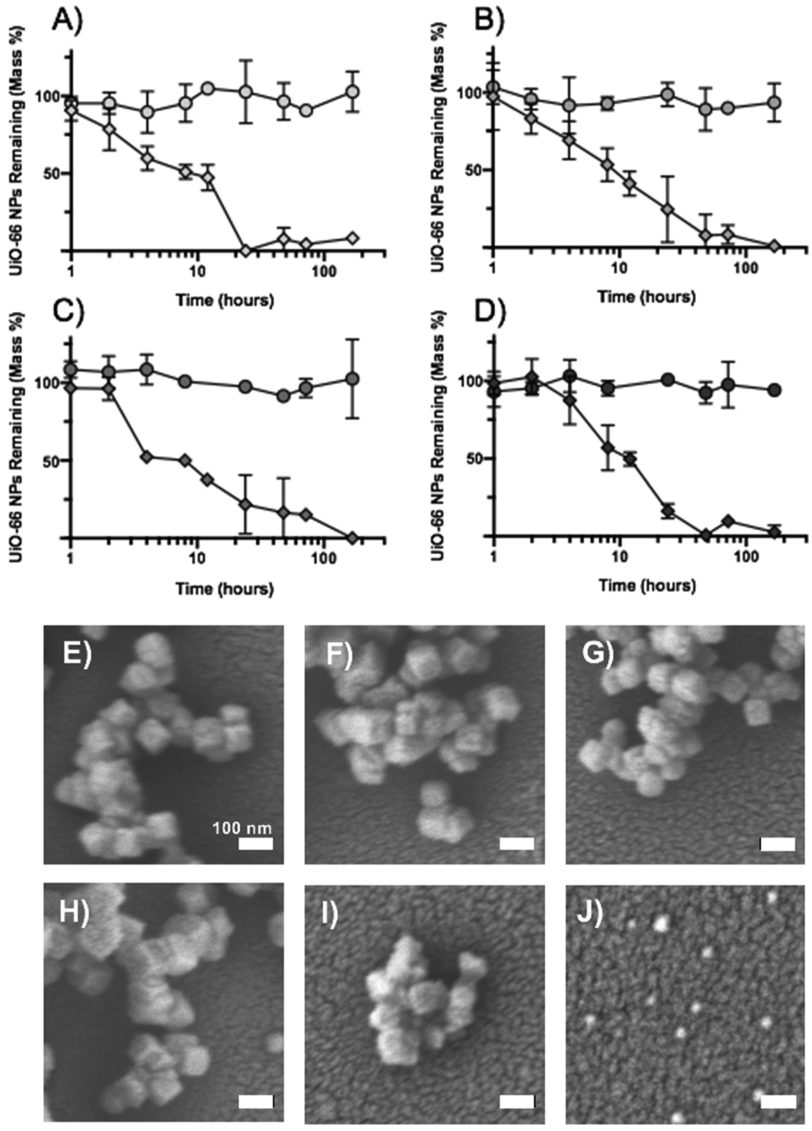

Figure 4. Degradation of UiO-66 NPs in ALF and PBS. Degradation of (A) 1, (B) 8, (C) 12, and (D) 15% defective UiO-66 NPs in ALF (diamonds) and in PBS (circles) over time. SEM images of 1% defective UiO-66 NPs in PBS after (E) 0, (F) 8, and (G) 48 h and in ALF after (H) 0, (I) 8, and (J) 48 h. Points represent the mean, and error bars represent standard deviation (n = 3).

equilibrium loading. The amount of cargo adsorbed is consistent with previous loading studies of similarly sized molecules in UiO-66, which observe adsorption amounts around 0.1 mg of cargo per mg of UiO-66, similar to the ∼0.15 mg of RhB per mg of UiO-66 found in this study and the ∼0.1 mg of dex per mg of UiO-66.[32] The amounts of RhB and dex adsorbed also compare well to reported small-molecule loading across a diverse range of MOFs.[33] The lack of difference in loading as a function of defectiveness for both cargo may be because the loading mechanism would be that of metal-ligand (M−L) bond breaking and reforming, which would have a kinetic effect during the incubation at 37 °C, but not an equilibrium effect, as pore volumes would not be significantly altered on the range of defectiveness studied.[34] This is also supported by the lack of acid used during the incubation, which could have facilitated Zr−O bond cleavage in the metal cluster. Another potential explanation is that there could be competing effects between the ability to retain adsorbed RhB/dex through the pi−pi stacking electron donor−acceptor interactions following diffusion into the pores of UiO-66 and the availability of additional pore volume into which RhB can adsorb because of the missing linkers, resulting in similar equilibrium loading amounts independent of defectiveness.[32,35]

Following the successful loading of UiO-66 NPs with cargo, the NPs were incubated in simulated biological fluids to determine their respective rates of release of the fluorescent cargo over time in environments mimicking extracellular (phosphate-buffered saline or PBS, pH 7.4) and intracellular (artificial lysosomal fluid or ALF, pH 4.4) conditions. Although not fully encompassing the mucus or extracellular lung fluid and surfactants, PBS has been used to mimic the extracellular pH environment, often approximated *in vitro* with salt solutions (PBS or Gamble's solution) at equivalent pH, while ALF has been used to mimic the pH environment found following internalization by cells such as alveolar macrophages.[36−38] Thus, this study aimed to determine the relative rates and extents of release of cargo in the lungs prior to and after internalization using the aforementioned simulated fluids. The low pH environment simulated by the ALF is primarily found in phagosomes or endosomes following internalization

https://dx.doi.org/10.1021/acsami.0c10900
ACS Appl. Mater. Interfaces 2020, 12, 38989−39004

via phagocytosis or various methods of endocytosis, especially following fusion with lysosomes, but is also similar to the low pH found in extracellular tumor microenvironments, which could be another target for delivery of chemotherapeutics.[36,39] The results of the release study (Figure 3) demonstrate that there is minimal cargo release in PBS and relatively rapid release of cargo in ALF. Over the course of the 6 day study, the UiO-66 NPs incubated in PBS only released 10−20% of their cargo while the NPs incubated in ALF released effectively all of the entrapped RhB after 8−12 h. The results also indicate that there are minimal differences in the release profiles of the MOFs as a function of defectiveness, as statistical analysis *via* ANOVA indicates that only 2.01% of the variation occurs as a result of differing levels of defectiveness and that there are no statistically significant differences between the release profiles at almost any of the time points. The only time points at which there are significant differences are at the 1 and 2 h time points, where the less defective NPs tended to have a greater amount released than the more defective NPs. This difference, coupled with the difference in release profiles as a function of pH, likely indicates that either ligand or cluster protonation is a key factor in the release of the RhB cargo. Because there is greater release in less defective particles at earlier time points, it points to the entrapment of cargo being linked to the presence of ligands, which agrees with the previous hypothesis that pi−pi stacking is a primary factor in adsorption, although hydrogen bonding interactions could also play a role in the adsorption as well. Accordingly, as more ligands are protonated and dissociate from the cluster, more of the RhB cargo will be released. This aligns well with the vast difference in release profiles between PBS and ALF as well, whose key difference is pH, although the buffer salts do differ somewhat as well. At lower pH (in ALF), more ligands will be protonated, which are then potentially outcompeted by anionic buffer components, leading to greater release of RhB. To confirm that the lower pH environment was likely causing protonation and breakdown of the MOFs, we elected to look further into the stability and rates of breakdown of the MOFs in both pH conditions.

UiO-66 Stability in Simulated Biological Fluids. The degradation of UiO-66 in PBS, which simulates an extracellular pH environment, and ALF, which simulates an intracellular environment, was determined over time *via* TGA (Figure 4A−D). As the results demonstrate, all formulations of UiO-66 NPs degrade much more rapidly in ALF than they do in PBS. This degradation, shown visually in the SEM images in Figure 4E−J, primarily occurs over the course of the first 24 h for all four levels of defectiveness. In contrast to the rapid degradation in ALF, none of the UiO-66 NPs show any significant signs of degradation over the course of a one-week time period when incubated in PBS. These results indicate that pH, as well as potentially differences in buffer components, is likely responsible for the differences in degradation in ALF and PBS. The degradation differences also align well with the observed release of cargo shown in Figure 3, which demonstrated rapid release of RhB cargo in ALF with minimal release in PBS. The results of this stability study affirm our hypothesis that breakdown of the UiO-66 NPs is requisite for most of the cargo release, as other mechanisms such as passive diffusion could have been at play to cause the release of RhB. This represents another advantageous property of UiO-66 for use in biological applications, as cargo will be retained while in the interstitium and will only be released when the NPs are internalized by cells. This will not only increase the efficacy of dosage, but also reduce off-target effects. Not only that, but pH-sensitive delivery vehicles have been used in pulmonary delivery for treatment of lung cancers and tuberculosis, making use of selective release when internalized by macrophages or encountering the low pH tumor microenvironment.[40,41] This UiO-66 NP vehicle has this functionality and is readily modifiable to add more functionalities such as stealth, active targeting, and controlled release *via* conjugation of additional moieties.[5,42,43]

The stark contrast in the rate and extent of degradation of the UiO-66 NPs in the two media suggests that the mechanism of the breakdown of the particles is the protonation of the carboxylic acid groups of the terephthalic acid linkers of the MOFs, as the protonation of the ligands would greatly weaken the previously strong metal-carboxylate bonds.[5,11,14,44] The degradation of the NPs aligns well with expectations based on the pK_a of the carboxylic acid groups on terephthalic acid, which are 4.46 and 3.54. Accordingly, at the pH of the ALF of 4.4, a much larger fraction of the terephthalic acid ligands would be expected to be protonated and thus able to dissociate from the metal cluster relative to those in PBS, which has a pH of 7.4. This pH difference would result in ∼1000 times fewer protons in solution, leading to far fewer terephthalic acid ligands being protonated in PBS than in ALF, aligning with the results, which indicate that UiO-66 is stable in PBS for up to a week and likely well beyond. This difference in degradation is also likely a function of solution pH, not the components of the buffers, because the main sources of acid for both simulated biological fluids are phosphate-based acids, which had previously been believed to displace the terephthalic acid ligands readily from the metal cluster, leading to the breakdown of the material.[6] Interestingly, our results contrast with similar UiO-66 stability studies performed by Lázaro, *et al.*, which indicated that members of the UiO-66 family of materials degrade over the course of hours in PBS at neutral pH, which may indicate that both protonation and charge-compensating ions are necessary to cause breakdown of the UiO-66 NPs.[5] This departure from previously observed results further underscores the importance of the synthesis method in the stability of the formed UiO-66, as the materials previously studied utilized acidic modulators in their syntheses and/or did not quantify the water present in the dimethylformamide (DMF) during synthesis.[5,6,11,14] The lack of acidic modulators in our syntheses may be strongly connected to the stability of the materials and persistence in phosphate-buffered media. That said, the concentration of UiO-66, the overall NP size, the components of the buffer (especially salt concentrations), and the pH all likely factor into the breakdown noted here, as previous studies have shown that pH alone does not lead to significant breakdown of UiO-66 as determined *via* powder X-ray diffraction and Fourier-transform infrared spectroscopy.[11]

Aerodynamic Sizing of UiO-66 NPs. Because lung penetration depth depends on the aerodynamic diameter (D_{ae}), robust aerodynamic characterization is critical in the design of pulmonary drug delivery systems.[22] We sized UiO-66 NPs of all levels of defectiveness from two aerosol devices (a Collision Jet Nebulizer or CJN and a Monodose dry powder inhaler or DPI) using a Next Generation Impactor (NGI). Aerosols formed from a CJN were utilized to evaluate the aerodynamics of individual UiO-66 particles, as rapid methanol evaporation following CJN nebulization yields distinct aerosol particles.[45] The residence time of aerosolized dispersions were determined to be long enough to ensure that methanol

https://dx.doi.org/10.1021/acsami.0c10900
ACS Appl. Mater. Interfaces 2020, 12, 38989−39004

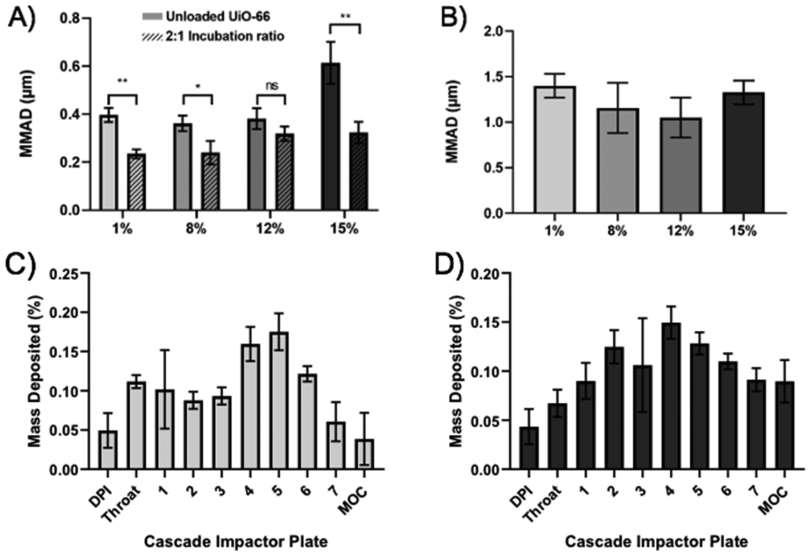

Figure 5. Aerodynamic characterization of UiO-66 NPs. (A) MMAD of unloaded and loaded UiO-66 NPs with varying defectiveness (1, 8, 12, and 15%). (B) MMAD of unloaded UiO-66 with varying defectiveness after dry powder aerosolization. (C) Mass deposition profile for 1% defective UiO-66 NPs from NGI impaction after dry powder aerosolization. (D) Mass deposition profile for 15% defective UiO-66 NPs from NGI impaction after dry powder aerosolization. Bars represent the mean, and error bars indicate standard deviation (n = 3), where * p-value < 0.05, ** p-value < 0.01, and ns is not significant as determined by Sidak's multiple comparisons as part of a two-way ANOVA.

evaporated per previous literature.[46] Unloaded UiO-66 NPs and UiO-66 NPs loaded with RhB at a 2:1 incubation ratio were aerosolized from a CJN to obtain the monodisperse mass mean aerodynamic diameter (MMAD) of the NPs. The results of the aerodynamic sizing (Figure 5A, full deposition profiles in Figures S7−S10) indicate that the unloaded UiO-66 NPs tend to have MMADs between 0.4 and 0.5 μm and that MMADs decreased when loaded with RhB cargo. Our results indicate that the observed decrease in MMAD when NPs were loaded with cargo was statistically significant for NPs with 1, 8, and 15% defectiveness, but was not for 12% defective NPs. Between defectiveness levels of unloaded UiO-66, the MMAD of unloaded UiO-66 NPs with 15% defectiveness was statistically larger than the less defective NPs, but there were no other significant differences among the 1, 8, and 12% particles, indicating that defectiveness has potential for modulation of MMAD. Between defectiveness levels of loaded UiO-66, differences in MMAD were not statistically significant. The observed aerodynamic diameters from this study fall into the desired range for deposition in the alveolar region of the lung, particularly when formulated into a dry powder, which increases the aerodynamic diameter of the particles to ∼1−1.5 μm.[22] This size range is more advantageous for deep lung penetration relative to other works utilizing aerosolized MOFs, which have reported MMADs of 0.42−0.59, 0.9 μm, and even as large as 4.46 μm.[16−18] Unlike the MMADs found in these other studies, the 1−1.5 μm size range found in this study indicates that this system could be feasibly applied as an inhalation delivery platform with consistent deep lung penetration.[22]

Particle D_{ae} are related to their D_{eq}, which is the geometric diameter of a spherical particle with an equivalent diameter, through the relationship of the particle density (ρ_p) and the shape factor (χ), which encompasses all aspects of non-spherical particle drag (eq 1).

$$D_{ae} = D_{eq}\sqrt{\frac{\rho_p}{\rho_0 \chi}} \quad (1)$$

Equation 1: formula for calculation of the aerodynamic diameter (D_{ae}) based on the equivalent particle diameter (D_{eq}), particle density (ρ_p), shape factor (χ), and unit particle density of 1 g/cm^3 (ρ_0).

Although particle density (ρ_p) would be expected to increase with cargo-loading of UiO-66 and lead to an increase in the MMAD of loaded NPs, the opposite trend is observed. The decreased MMAD for loaded UiO-66 demonstrates that an increase in shape factor (χ) also occurs during cargo-loading, driving the observed reduction in the overall MMAD. As no significant topological differences were observed between SEM images of loaded and unloaded NPs (Figure 1), the particle surface roughness and macroscopic particle shape are not expected to be the primary contributors toward increasing χ. However, an increase in shape factor (χ) could arise from variations in internal airflow through UiO-66 pores, increasing the drag forces felt on loaded NPs, especially if the loading generates uneven air flows within the particle. Overall, the high degree of tunability in MMADs of UiO-66 NPs suggests that leveraging the parameters that control defectiveness, geometric size, and cargo-loading can allow for modulation of the aerodynamic diameter, giving improved control over nuanced pulmonary targeting *in vivo*.

While CJN nebulization is a useful tool for analyzing individual particle dynamics, delivery *via* dry powder inhalation is preferred clinically and will yield more representative inhalation powders.[47] When formulated into a dry powder, the MMADs of UiO-66 NPs increase to around 1 μm, with no significant differences between D_{ae} at each defectiveness level (Figure 5B, full deposition profiles in Figure 5C,D). The observed increase in MMAD from the dry powder formulation likely occurs because of particle aggregation driven by van der Waals forces that are enabled during lyophilization and lead to incomplete dispersion during the aerosolization processes.

https://dx.doi.org/10.1021/acsami.0c10900
ACS Appl. Mater. Interfaces 2020, 12, 38989−39004

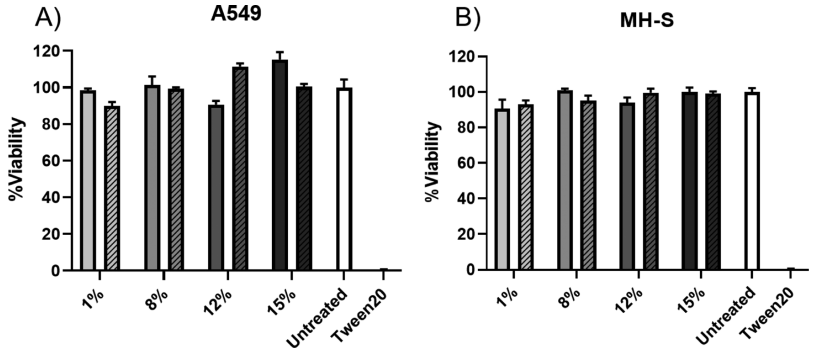

Figure 6. Cell viability of cell lines following UiO-66 NP treatment. 24 h cell viability of (A) A549 and (B) MH-S cell lines. Solid bars under the 1, 8, 12, and 15% conditions represent treatment with 1 μg/mL of UiO-66 NPs, while patterned bars represent treatment with 50 μg/mL of UiO-66 NPs. Bars represent the mean and error bars represent standard error (n = 3). All groups are not statistically significant compared to the untreated conditions (p-value > 0.05) as determined by Dunnett's multiple comparisons test as part of a two-way ANOVA.

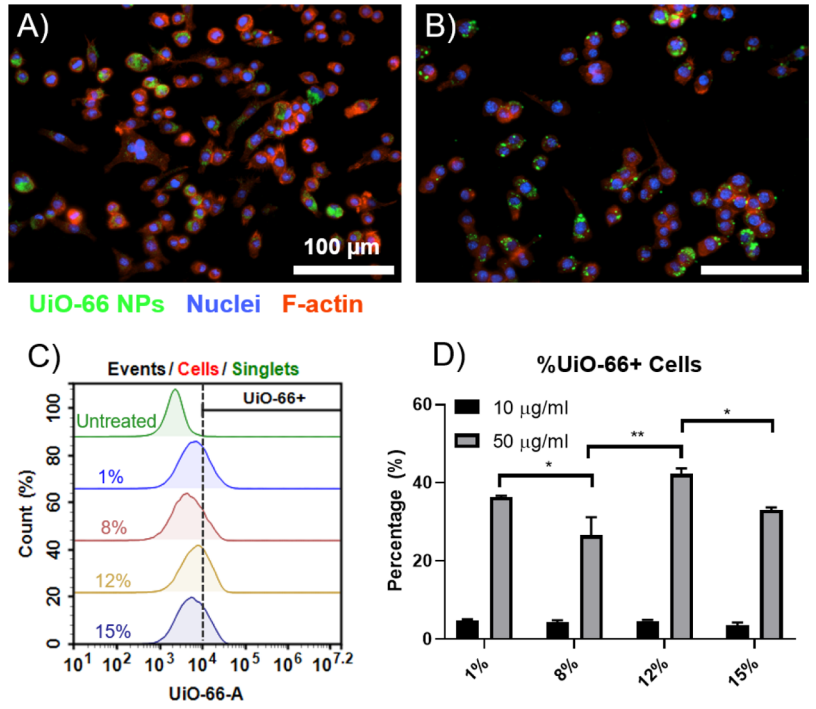

Figure 7. MH-S cellular uptake of UiO-66 NPs. Fluorescent imaging of cells treated for 24 h with 50 μg/mL UiO-66 NPs of (A) 1% defectiveness or (B) 15% defectiveness. (C) Histograms of flow cytometric NP uptake analysis of cells treated with 50 μg/mL of UiO-66 NPs of various levels of defectiveness determined using median fluorescence intensity of UiO-66. Treatment conditions are indicated on the plot to the left of the histograms. (D) Quantitative uptake with flow cytometry at two concentrations of UiO-66 NPs. Bars represent the mean and error bars represent standard error (n = 3). *p-value < 0.05, **p-value < 0.01 as determined by Tukey's multiple comparisons test as part of a two-way ANOVA.

However, fine particle fractions (FPFs), which measure the proportion of particles sized under 5 μm, ranged from 0.75–0.81 for dry powder UiO-66 formulations, comparing favorably to other NP aerosol systems, where other work reported FPFs of 0.31 and 0.57, and some clinical platforms operate at FPFs of 0.26.[16,17,48] Additionally, emitted doses (ED), a measure of the proportion of particles that actually enter the lung, ranged from 0.94–0.96, indicating the efficacy benefits offered by dry powder formulations of these NPs. These MMADs were obtained uniquely for neat, excipient-free UiO-66 NP powders, highlighting the utility of these monodisperse particles for effective for aerosol delivery and deep lung penetration. MMADs of this size range are ideal for many deep lung delivery applications, while the high ED and FPF point to dry powder formulations with considerably large deposition efficiencies.[22] A table with full aerosol characterization of the NPs for both CJN and dry powder formulations can be found in Table S2.

***In Vitro* Uptake and Biocompatibility of UiO-66 NPs in Lung Cells.** Utilizing MOFs as pulmonary drug delivery vehicles requires that the vehicle itself does not cause any undesirable cytotoxicity in the lung. To assess the acute cytotoxicity of UiO-66 NPs of various levels of defectiveness *in vitro*, we studied the interactions of UiO-66 NPs with two relevant cell lines representing lung epithelial and pulmonary immune cells. A549 alveolar basal epithelial cells and MH-S alveolar macrophages were treated with 1 and 50 μg/mL UiO-66 NPs and cell viability was assessed at 4 and 24 h timepoints using CellTiter-Glo 2.0 Luminescent assay for both cell lines. Treatment of UiO-66 NPs of various defectiveness levels at

https://dx.doi.org/10.1021/acsami.0c10900
ACS Appl. Mater. Interfaces 2020, 12, 38989–39004

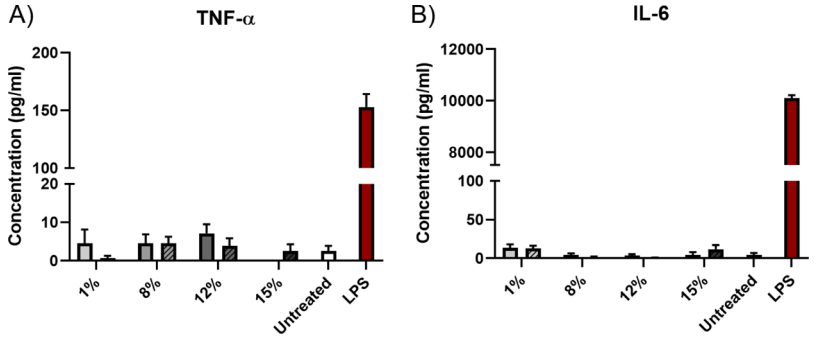

Figure 8. Inflammatory cytokine production in MH-S cells. 24 h secretion of (A) TNF-α and (B) IL-6. Solid bars under the 1, 8, 12, and 15% conditions represent treatment with 1 μg/mL of UiO-66 NPs, while patterned bars represent treatment with 50 μg/mL of UiO-66 NPs. Bars represent the mean and error bars represent standard error (n = 3). All groups are not statistically significant compared to the untreated conditions (p-value > 0.05) as determined by Dunnett's multiple comparisons test as part of a two-way ANOVA.

either 1 μg/mL (solid bars) or 50 μg/mL (patterned bars) of UiO-66 NPs did not result in any significant loss of cell viability in A549 cells at the 4 h (Figure S13) and the 24 h timepoints (Figure 6). No significant decline in cell viability was observed for any of the four tested defectiveness levels as compared to the viability of untreated cells as determined *via* Dunnett's multiple comparisons test as part of a two-way ANOVA. Cell viability was maintained at both timepoints, indicating strong biocompatibility and safety of UiO-66 NPs as a drug nanocarrier to epithelial and immune cells in the lung. Cell viability of A549 and MH-S cells closely matches previous reports of UiO-66 biocompatibility with other cell types,[49,50] suggesting minimal cytotoxicity of the UiO-66 nanocarrier itself. UiO-66 NPs provide a potential advantage over other types of MOFs, including some iron-based MOFs that showed notable cytotoxicity in pulmonary cells.[51] These results expand the use of UiO-66 NPs from anti-cancer and chemotherapeutic delivery applications to broad drug delivery to a range of cell and tissue types, as the low cytotoxicity of UiO-66 NPs closely resembles that of commonly used, biocompatible polymeric NPs.[52]

Because of the proficiency of alveolar macrophages in clearing particulates, we assessed the uptake of UiO-66 NPs *in vitro* with MH-S cells. Fluorescein isothiocyanate (FITC)-loaded UiO-66 NPs of various levels of defectiveness were dosed to MH-S cells and incubated for 24 h. MH-S cells were readily capable of internalizing UiO-66 NPs of all defectiveness levels as indicated by the presence of cells bearing green fluorescent signal in the fluorescent microscopy images (Figure 7A,B). Because of the rapid degradation of UiO-66 NPs in intracellular environments, it is expected that the breakdown of FITC-loaded UiO-66 NPs will lead to cargo release after internalization. Accordingly, we observe increased diffuse intracellular fluorescence following cellular uptake of both 1 and 15% UiO-66 NPs. To distinguish between internalized and cell−surface bound NPs, quenching with Trypan Blue dye was performed on MH-S cells treated with FITC-loaded UiO-66 NPs of 1 and 15% defectiveness (Figure S14). Fluorescent imaging revealed that FITC signal was retained following Trypan Blue quenching in both 1 and 15% NPs, indicating that the majority of UiO-66 NPs was internalized by MH-S cells rather than bound to the cell surface. Cellular uptake of unloaded UiO-66 NPs was confirmed *via* flow cytometric analysis (Figure 7C,D). Utilizing the inherent UV fluorescence of unloaded UiO-66 NPs as previously described,[25] analysis of MH-S cell uptake revealed approximately 5% of MH-S cells were associated with UiO-66 NPs at the low concentration of 10 μg/mL of UiO-66 NPs and a range of 27−42% MH-S cell uptake at the higher concentration of 50 μg/mL, which varied with UiO-66 NP defectiveness. The uptake results reflect similar uptake patterns to other MOFs in alveolar macrophages,[53] although the absolute number of cells detected as UiO-66 NP+ was lower than studies of UiO-66 NPs in other systems.[12,54] UiO-66 NP uptake may be lower than expected because of the rapid breakdown of the NP framework in intracellular environments, leading to a lower detected signal of the inherent fluorescence. In addition, UiO-66 NPs showed relatively low fluorescence regardless of the photomultiplier tube voltage, which explains differences in internalization between fluorescent imaging and flow cytometric uptake data (Figure 7A,B,D) and could account for the statistical differences in uptake for NPs of different defectiveness (Figure 7D) according to two-way ANOVA with Tukey's multiple comparisons test. Nevertheless, treatment of unmodified UiO-66 NPs at relatively modest amounts yielded strong uptake by murine alveolar macrophages. UiO-66 NPs are expected to be internalized by professional phagocytic MH-S cells through actin-dependent macropinocytosis and phagocytosis pathways, which is the case for other similar sized MOF NPs in swine alveolar macrophages.[53]

Following internalization of foreign material, alveolar macrophages can become activated and respond by secreting inflammatory cytokines intended to recruit lymphocytes to address danger signals. We assessed the inflammatory response of MH-S alveolar macrophages to the treatment of UiO-66 NPs with varying levels of defectiveness. Lipopolysaccharide (LPS), a cell wall component of Gram-negative bacteria and a toll-like receptor 4 (TLR4) agonist was used as a positive control for inflammation. In general, notably low levels of tumor necrosis factor (TNF)-α and interleukin (IL)-6 pro-inflammatory cytokines in MH-S culture supernatants were observed at timepoints of 4 h (Figure S15) and 24 h (Figure 8) following UiO-66 NP treatments at 1 and 50 μg/mL NP concentrations. Furthermore, TNF-α and IL-6 inflammatory cytokine secretion was not statistically different in any UiO-66 sample from those of untreated cells according to a two-way ANOVA with Dunnett's multiple comparisons test (p-value > 0.05), indicating low immunogenicity of UiO-66 NPs of all defectiveness levels. UiO-66 NPs of all treatments and defectiveness levels show drastic statistical differences when compared to LPS treatments according to a two-way ANOVA with Dunnett's multiple comparisons test (p-value < 0.0001).

https://dx.doi.org/10.1021/acsami.0c10900
ACS Appl. Mater. Interfaces 2020, 12, 38989−39004

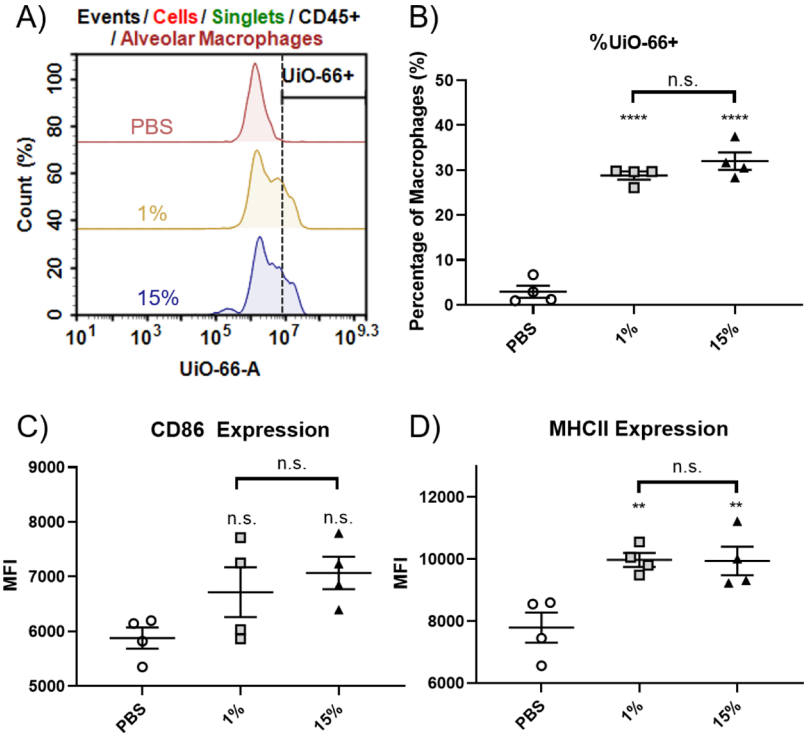

Figure 9. BALF alveolar macrophage uptake and activation markers. (A) Histograms of flow cytometric NP uptake analysis of alveolar macrophages determined using median fluorescence intensity of UiO-66. Treatment conditions are indicated on the plot to the left of the histograms (B) quantitative UiO-66 NP uptake by alveolar macrophages using flow cytometry. (C) CD86 expression of alveolar macrophages. (D) MHCII expression of alveolar macrophages. Lines represent the mean and error bars represent standard error ($n = 4$). *p-value < 0.05, **p-value < 0.01, ****p-value < 0.0001, and n.s. not significant as determined by Tukey's multiple comparisons test as part of a one-way ANOVA.

The negligible levels of inflammatory cytokines caused by UiO-66 NP treatment, which are indistinguishable from levels of cytokines secreted by untreated cells, are additional proof for the strong biocompatibility of UiO-66 NPs with pulmonary cells. To our knowledge, this is the first assessment of the impact of UiO-66 NPs on inflammatory cytokine secretion in alveolar macrophages. While UiO-66 has not been previously assessed in great detail for inflammatory cytokine response in macrophages, our results of low inflammatory cytokine secretion following UiO-66 NP treatment are in agreement with studies of other MOFs interacting with RAW264.7 macrophages, which show negligible secretion of inflammatory cytokines due to the administration of the blank MOF vehicle.[55]

***In Vivo* Uptake, Biocompatibility, and Biodistribution of UiO-66 NPs.** To evaluate the impact of a uniform dose of UiO-66 NPs on potential lung inflammation following pulmonary delivery, we dosed 6−8 week-old female C57BL/6J mice with 100 μg of UiO-66 of either 1 or 15% defectiveness *via* orotracheal instillation. At a timepoint of 24 h, a bronchoalveolar lavage (BAL) was performed and the bronchoalveolar lavage fluid (BALF) was analyzed to assess potential inflammation and recruitment of inflammatory cells in the airways. Flow cytometry was also used to assess alveolar macrophage (CD45+/Ly6G-/Siglec-F+) uptake of UiO-66 NPs to elucidate the *in vivo* fate of UiO-66 NPs (Figure 9A,B). Approximately 30% of alveolar macrophages in the BALF were measured to be positive for UiO-66 NPs; 29 and 32% for UiO-66 NPs of 1 and 15% defectiveness, respectively. There was no statistical difference between the uptake levels of UiO-66 NPs of different defectiveness according to Tukey's multiple comparisons test as part of a one-way ANOVA, which indicates that defectiveness does not play an important role in determining uptake by macrophages in the lung. The uptake levels fall in the range of *in vitro* uptake as determined by flow cytometric analysis of MH-S cells, indicating good agreement between *in vitro* and *in vivo* analyses of UiO-66 NP interactions with murine pulmonary immune cells. Similar to *in vitro* results, detected UiO-66 NP uptake results seem lower than previous reports of alveolar macrophage uptake of other NPs of a similar size,[56,57] which may be due to the degradation of the UiO-66 NP framework in the first hours following internalization or due to the low inherent fluorescence of UiO-66 NPs as seen in *in vitro* analyses of uptake in MH-S cells. UiO-66 NPs are expected to mostly be internalized by alveolar macrophages following pulmonary administration, as is the case with other unmodified particles, while a small fraction of NPs will associate with alveolar epithelial cells.[57,58] In addition, the negative surface charge on UiO-66 NPs is likely to increase association with macrophages relative to other cells.[59]

To determine the phenotypical implications of UiO-66 NP uptake by alveolar macrophages, we elected to test the expression of two surface proteins: CD86, a marker associated with classically activated macrophages of a proinflammatory phenotype, and major histocompatibility complex class II (MHCII). CD86 expression was not statistically significantly elevated in alveolar macrophages of mice treated with UiO-66 NPs of 1 and 15% defectiveness levels relative to untreated mice *via* Tukey's multiple comparisons test as part of a one-way ANOVA (Figure 9C). This indicates the low potential of UiO-66 NPs to drive an undesirable proinflammatory activation in alveolar macrophages *in vivo*. MHCII expression, however, was significantly enhanced in alveolar macrophages of

https://dx.doi.org/10.1021/acsami.0c10900
ACS Appl. Mater. Interfaces 2020, 12, 38989−39004

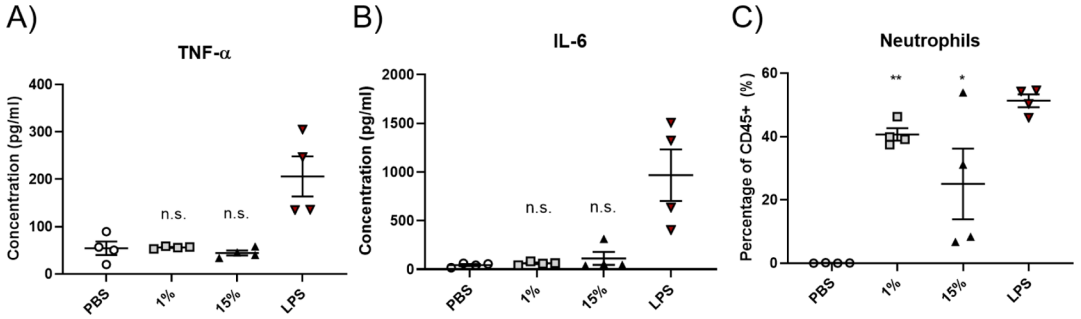

Figure 10. Inflammatory analysis of BALF. 24 h secretion of (A) TNF-α and (B) IL-6 inflammatory cytokines in the BALF. (C) Percentage of neutrophils of all CD45+ populations in the BALF. Lines represent the mean and error bars represent standard error ($n = 4$). *p-value < 0.05, **p-value < 0.01, and n.s. not significant compared to the PBS conditions as determined by Dunnett's multiple comparisons test as part of a one-way ANOVA.

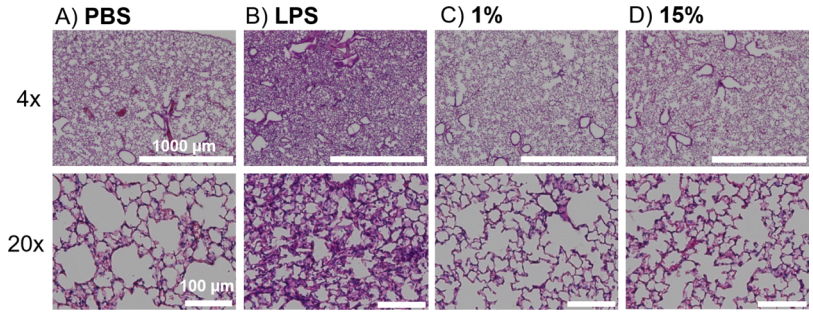

Figure 11. Histological analysis of lungs from mice treated with UiO-66 NPs. H&E-stained lung sections of mice treated with (A) PBS, (B) LPS, (C) 1% UiO-66 NPs, and (D) 15% UiO-66 NPs. The top row represents images of lung sections taken at a 4× magnification, and the bottom row represents images of lung sections taken at a 20× magnification.

mice treated with UiO-66 NPs of both 1 and 15% defectiveness levels with a p-value < 0.01 as determined by Tukey's multiple comparisons test as part of a one-way ANOVA (Figure 9D). In general, alveolar macrophages are considered an unattractive target for vaccines and immunotherapies relative to pulmonary dendritic cell populations because of their low inherent MHCII expression and poor potential to activate helper T cells.[60] Pulmonary administration of UiO-66 NPs primed the upregulation of MHCII without inducing any changes towards a proinflammatory phenotype, highlighting the potential for using UiO-66 NPs as drug delivery vehicles for immune engineering applications in the lung.

To further confirm the minimal inflammatory effects of UiO-66 NPs in the lung, we measured the levels of IL-6 and TNF-α inflammatory cytokines in the BALF. No statistically significant increase in IL-6 or TNF-α levels in BALFs was observed in mice dosed with either 1 and 15% defectiveness UiO-66 NPs as compared to mice dosed with PBS *via* Dunnett's multiple comparisons test as part of a one-way ANOVA (Figure 10A,B). On the other hand, levels of IL-6 and TNF-α in the two groups of UiO-66 NP-treated mice were statistically lower when compared to the LPS-treated group (p-value < 0.01) as determined by another Dunnett's multiple comparisons test. These results and patterns are in good agreement with *in vitro* inflammatory cytokine levels and indicate the low immunogenicity of UiO-66 NPs in the pulmonary space. The negligible BALF levels of IL-6 and TNF-α caused by UiO-66 NPs are comparable to those in previously reported biocompatible polymer-based NP formulations used in pulmonary drug delivery, namely poly(ethylene glycol) (PEG) and poly(lactic-*co*-glycolic acid).[61,62] UiO-66 NP formulations offer an advantage over polymeric NPs in pulmonary applications because of the NPs' high porosity and controlled defectiveness, which allow for controlled deposition in the alveolar region of the lung as well as high loading and delivery of cargo.

Despite the low levels of proinflammatory cytokines, UiO-66 NPs caused an increase in the number of neutrophils (identified as CD45+/Ly6G+/Siglec-F−) in the BALF, with averages of 40 and 25% of all CD45+ cells for mice treated with UiO-66 NPs of 1 and 15% defectiveness levels, respectively (Figure 10C). This may be a potential drawback to using UiO-66 NPs because neutrophil presence is not usually observed for biocompatible polymeric NPs in the pulmonary space.[62] While the neutrophil counts are elevated, they remain below the neutrophil percentages in LPS-treated mice, which are about 51% on average. Given the low inflammatory profile in the lungs of UiO-66 NP-treated mice as shown by cytokine analysis and cellular markers, it is probable that the higher than expected presence of neutrophils in samples could be due to the presence of trace amounts of blood in the BALF during the lavage extraction process. This is corroborated by histological analysis; we observe that lung sections of UiO-66 NP-treated mice are visually indistinguishable from those of PBS, the negative control, with respect to cellularity and the presence of infiltrating inflammatory cells (Figure 11). The low levels of airway inflammation are reflected in mice treated with both UiO-66 NP groups, 1 and 15% defectiveness. A starkly different effect is observed in LPS-treated mice in which acute airway inflammation is evident through the presence of a significant number of infiltrating inflammatory cells. These results indicate that UiO-66 NP treatment does not cause any notable inflammation of the airways, suggesting the low pulmonary immunogenicity of

https://dx.doi.org/10.1021/acsami.0c10900
ACS Appl. Mater. Interfaces 2020, 12, 38989−39004

UiO-66 NPs. Furthermore, the histological results confirm that UiO-66 NPs cause a considerably smaller number of infiltrating cells relative to LPS. Hematoxylin & Eosin (H&E) staining of UiO-66 NP-treated lungs closely resembles cellularity and low inflammation seen in many biocompatible biomaterials including several formulations of polymeric NPs,[57,62] indicating the robust biocompatibility of UiO-66 NPs of different defectiveness levels, especially in the airways and alveolar space. These results are also comparable to studies involving the *in vivo* interactions of other types of MOF and normal tissue architecture in different organs.[63]

Because of the low inherent fluorescence of the UiO-66 NPs in histological sections limiting direct evaluation, biodistribution *via* inductively-coupled plasma mass spectrometry (ICP–MS) analysis of digested organs was performed to determine the relative localization of the 1% defective (Figure 12A) and

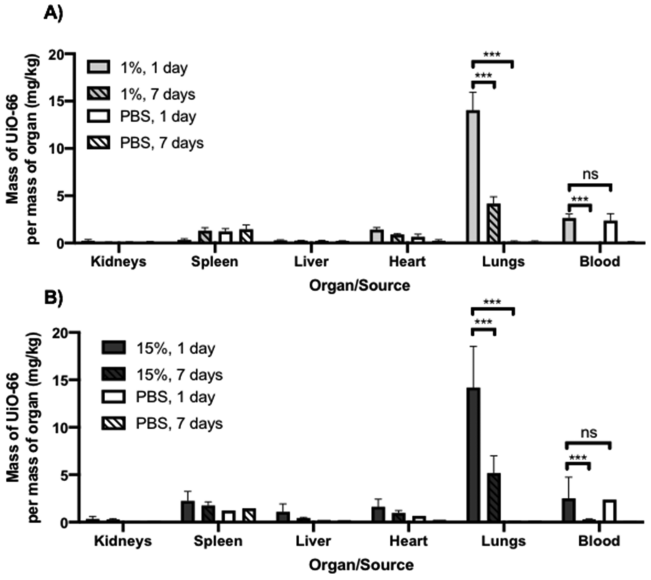

Figure 12. Biodistribution of equivalent mass of UiO-66 in various organs and blood. The two treatments shown are for 1% defective UiO-66-treated and PBS-treated mice at 1 and 7 day time points. Error bars represent standard error (n = 4). ***p-value < 0.001 *via* Sidak's multiple comparisons test.

15% defective (Figure 12B) MOFs at 1 and 7 day time points. The results of this study demonstrate not only that the UiO-66 NPs localize to the lungs 24 h after instillation, but also that the NPs are cleared from the body to a significant extent after a 7 day time period. This is a key result, as pulmonary delivery leads to high local lung concentrations and rapid clearance in the lungs. Pulmonary delivery avoids pathways of IV injection, which route the NPs to clearance organs such as the liver or spleen, or, ultimately, to lymph nodes, as observed for similar sized NPs of different compositions.[64,65] This clearance over the course of a week is a critical step for use of UiO-66 in biomedical applications because it demonstrates that although the material is stable in neutral pH aqueous environments found in the body, it will break down and be cleared from the lung, likely after cellular uptake, precluding potential complications from long-term accumulation.[66] For UiO-66 NPs not taken up by pulmonary cells, they will likely nonspecifically diffuse into the blood or be trafficked to lymph nodes, two common pathways for NP transport following pulmonary administration.[67] The results of this study, however, indicate that the levels of Zr found in the blood and in the heart are not elevated relative to the PBS control as determined by Sidak's multiple comparisons test, indicating that the UiO-66 NPs are retained in the lungs before being cleared gradually over time and are not lost to leakage into blood or other organs. This contrasts with other cases in which nondegradable particles have been found internalized within macrophages for over a month,[57] but may indicate that, because of the negative charge of UiO-66 (measured to be −15 to −25 mV), they are preferentially internalized by phagocytic cells and thus remain in the lungs.[29] Our results are similar to those found for pulmonary delivery of 100 nm albumin particles to rats, which showed good lung retention prior to clearance over a similar time frame, highlighting the significance of the degradable UiO-66 framework.[68] The accumulation and clearance of the UiO-66 NPs was also determined to not be a function of the defectiveness of the NPs, a beneficial property of the material, as batch-to-batch differences in defectiveness will still yield consistent, predictable delivery to the lung, a critical property for pulmonary drug delivery. These results, combined with the stability UiO-66 in extracellular-mimicking environments, cargo release in intracellular-mimicking environments, advantageous aerosol properties for deep lung deposition, and biocompatibility indicate that these size-controlled UiO-66 NPs are promising candidates for pulmonary drug delivery vehicles.

CONCLUSIONS

In this study, we evaluate the utility of UiO-66 MOF NPs as pulmonary drug delivery vehicles by investigating their aerodynamic properties upon aerosolization, cargo loading and release profiles, degradability in extracellular and intracellular-mimicking environments, and biocompatibility with lung cell lines and murine *in vivo* models. We examine UiO-66 NPs of different defectiveness levels, which all show high capacity for loading, as well as rapid release of cargo in low pH, intracellular-mimicking environments. UiO-66 NPs can be readily degraded intracellularly because of the ease of linker protonation at lower pH under biologically relevant conditions. Degradability is a necessary property of any drug delivery carrier especially in the pulmonary space, which was also demonstrated through the rapid clearance of zirconium from the lungs over the course of one week. This result in particular is critical to a material such as UiO-66, which is typically considered to be quite robust and resistant to breakdown. *In vivo* biocompatibility and clearance highlight the great potential for uses in biomedical and pulmonary-specific applications. While there were minimal statistical differences in loading, release, clearance, and biocompatibility that occurred as a result of varying UiO-66 NP defectiveness, we did observe differences in aerodynamic diameters across NPs of different defectiveness groups, especially upon cargo loading. This points to an opportunity to control NP deposition in the lung, a critical feature for a pulmonary drug delivery platform. The lack of differences as a function of defectiveness are also an advantageous feature for pulmonary drug delivery, as inconsistencies in terms of dosage frequently occur because of variable properties (size, loading, release, distribution) of the delivery vehicle. This study underscores the robust consistency of UiO-66 independent of defects, which will preclude these issues of inconsistency which plague many current pulmonary drug delivery formulations. Fur-

https://dx.doi.org/10.1021/acsami.0c10900
ACS Appl. Mater. Interfaces 2020, 12, 38989−39004

thermore, UiO-66 NPs showed remarkable biocompatibility both *in vitro* with murine and human lung cells and *in vivo* in a mouse model. They also did not cause any notably undesirable interactions in the lung, demonstrating low cytotoxicity and negligible levels of secreted inflammatory cytokines.

The results presented in this work represent the first step in the use of MOFs for inhalable drug delivery to the lung. Future work may explore implementation of additional MOF materials based on biocompatible and/or endogenous metals for pulmonary delivery. Interactions of UiO-66 NPs in human lungs have yet to be investigated, but we expect good biocompatibility and rapid clearance of the MOFs because of their degradability in intracellular and low pH environments. Furthermore, postsynthetic modifications such as PEGylation may also be employed to improve interactions with lung surfactant proteins, allow for more rapid diffusion through the mucus encountered upon deposition in upper airways, and limit internalization by macrophages in situations where uptake is not desirable. Future studies evaluating a wider range of therapeutic cargo delivery will be needed to assess potential dosages for human translation.[19,22,23] Overall, this study highlights the potential use of UiO-66 NPs in developing aerosol formulations for the delivery of therapeutic agents to the lung.

METHODS

Synthesis of UiO-66 NPs. The syntheses of UiO-66 NPs were performed as previously described.[25] Four preparations were utilized for experiments in these studies, as is noted in Table 2 below. $ZrCl_4$ (90.0 mg, 0.386 mmol) and terephthalic acid (H_2bdc, 1,4-benzenedicarboxylic acid, amount variable; see Table 2 for each sample) were added to 15 mL of anhydrous DMF along with a known amount of deionized H_2O (50 μL or 2.78 mmol) in a 20 mL vial and dissolved *via* sonication. Once the solution was clear, it was then heated at the temperature denoted in Table 2 for 24 h (h). The respective samples were then centrifuged, the supernatants were decanted, and the isolated powders were soaked in DMF for 72 h, replacing the solvent every 24 h. This was followed by a similar washing procedure with methanol. All washes were performed at room temperature.

Table 2. List of Synthesis Conditions of Samples Used in Studies[a]

sample (%)	mass of H_2bdc (mg)	mmoles of H_2bdc	temperature (°C)
1	128.2	0.772	110
8	64.1	0.386	110
12	64.1	0.386	100
15	51.3	0.309	110

[a]The sample names refer to the measured defectiveness as determined *via* TGA (described in the TGA Defectiveness section).

Dynamic Light Scattering. Dynamic light scattering (DLS) was performed using a Malvern Zetasizer Nano S following additional washing steps. As synthesized UiO-66 samples were washed in DMF three times prior to DLS measurement to remove any adsorbed terephthalic acid remaining in the pores of the MOFs. The washing procedure involved centrifugation at 18.2K RCF for 10 min followed by removal of the supernatant and redispersion into DMF using sonication. The UiO-66 sample concentrations were then adjusted to 0.1 mg/mL following concentration determination *via* TGA. DLS measurements were then performed to determine the hydrodynamic diameters (D_h) and polydispersity indices for each sample. Reported measurements for each defectiveness level were averages taken from three samples synthesized at the same synthetic conditions.

Zeta Potential. Zeta potential measurements were performed using a Malvern Zetasizer Nano ZS following additional washing steps, similar to DLS. As synthesized UiO-66 samples were washed in DMF three times, and deionized (DI) water three times prior to dispersion into 10 mM NaCl for zeta potential measurement to remove any adsorbed terephthalic acid remaining in the pores of the MOFs and redisperse into the aqueous medium without any solvent remaining. The washing procedure involved centrifugation at 18.2K RCF for 10 min followed by removal of the supernatant and redispersion into DMF/water/NaCl solution using sonication. The UiO-66 sample concentrations were then adjusted to 0.1 mg/mL following concentration determination *via* TGA. Zeta potential measurements were then performed to determine the effective surface charge of the UiO-66 NPs.

Scanning Electron Microscopy. Scanning electron microscopy (SEM) was performed using a JSM F7400 scanning electron microscope after each of the samples was sputter coated with gold/palladium using a Denton Desk IV sputter coater. The sizes (in this case, the geometric diameters, D_g) of the UiO-66 NPs were determined using the ImageJ program to manually determine the D_g of at least 50 NPs.

TGA Defectiveness. Defectiveness analysis was performed using TGA using a TA Q5000 SA. 10 mg or more of UiO-66 was loaded onto a tared aluminum pan and heated to 350 °C at a rate of 10 °C per min under a nitrogen atmosphere. The temperature was then held at 350 °C for 30 min to ensure complete DMF evaporation. The sample was then cooled to 250 °C where the atmosphere was switched to oxygen and the sample was heated to 600 °C at a rate of 3 °C per minute to combust the organic ligand present. The mass of the resulting ZrO_2 was compared to the mass of the dehydrated MOF to determine the defectiveness of the sample.[13]

TGA Concentration. UiO-66 NP concentrations in their dispersions in water or DMF were determined *via* TGA using a TA TGA 550. For dispersion into PBS, the concentration was determined in water, and NPs were then isolated *via* centrifugation at 18.2K RCF, water removed, and dispersed into PBS. A known volume of the dispersion was heated to either 120 °C (for water) or 165 °C (for DMF) to evaporate all solvent present. The temperature was then held for 15 min to ensure complete evaporation and removal of solvent from the pores of the structure. This remaining mass was deemed to be UiO-66, whose mass was recorded to determine the mass concentration in solution.

Gas Adsorption. Following washing in solvent, the respective solvated powders were dried under flowing nitrogen. Low-pressure gas adsorption isotherms were measured on a Micromeritics Tristar II PLUS at 77 K. UiO-66 was loaded into a gas adsorption tube and degassed overnight at 100 °C under flowing nitrogen. Upon activation the sample was analyzed with nitrogen at 77 K.

Cargo Loading and Release. UiO-66 NPs at 1 mg/mL were postsynthetically loaded with fluorescent cargo (rhodamine B, denoted RhB) or dex *via* incubation of UiO-66 with RhB or dex at 37 °C and shaking at 1000 rpm for 24 h. The incubation was performed in DMF with incubation ratios (mass of RhB or dex relative to mass of UiO-66) varying from 0.5:1 to 1:1 and was followed by removal of the supernatant of RhB/dex that remained in solution after centrifugation to isolate the cargo-loaded particles. The NPs loaded with RhB/dex were then washed an additional time with 1 mL DMF to remove excess RhB/dex.

Following loading, a subset of the loaded NPs (with a 1:1 incubation ratio and 1 mg/mL UiO-66) were re-dispersed into one of two media: PBS, pH 7.4, or ALF (composition in Table S1), pH 4.4.[36] After dispersion into one of the two respective media, the dispersions of cargo-loaded UiO-66 were incubated at 37 °C and shaken at 1000 rpm. At 0, 1, 2, 8, 12, 24, 48, and 144 h time points, 110 μL of aliquots were removed, remaining particles isolated *via* centrifugation, and supernatants analyzed *via* fluorescence to detect the amount of RhB released.

UiO-66 Stability in Simulated Biological Fluids Over Time. To evaluate the stability of UiO-66 in biologically-relevant conditions, samples of UiO-66 at all levels of defectiveness were dispersed into DI

https://dx.doi.org/10.1021/acsami.0c10900
ACS Appl. Mater. Interfaces 2020, 12, 38989−39004

water three times and then dispersed into either PBS or ALF at 1 mg/mL. These dispersions were then incubated at 37 °C and shaken at 1000 rpm. Aliquots of 100 μL of the samples were removed at 0, 1, 2, 4, 8, 24, 48, 72, and 168 h, spun down in a centrifuge at 18.2K RCF, re-dispersed into water, and their concentrations measured *via* TGA. The remaining mass was determined to be nondegraded UiO-66 NPs, similar to the method utilized in previous work.[69]

NGI Sizing. The aerodynamic diameter of unloaded and cargo-loaded UiO-66 particles (at a 2:1 incubation ratio) were measured using cascade impaction in a Copley NGI. Two apparatuses were used to aerosolize the particles: a CJN and a PlastiApe Monodose dry powder inhaler (DPI). For the CJN, aqueous dispersions of UiO-66 at 1 mg/mL were centrifuged at 18.2 RCF for 10 min and then re-dispersed in methanol three times. The dispersion was diluted into 30 mL of methanol and loaded into the CJN. Compressed air was fed into the nebulizer at 60 L/min to aerosolize the particle dispersion with methanol evaporation occurring rapidly to yield monodisperse UiO-66 aerosols from the CJN. For the Monodose DPI, dry powders of each unloaded UiO-66 sample were generated following lyophilization of aqueous particle dispersions. 10 mg of UiO-66 dry powder was loaded into a size 3 gelatin capsule and dispersed from the DPI. For both dispersion devices, the NGI was operated at 60 L/min for 100 s to ensure sufficient mass accumulation on the impactor stages. UiO-66 particles were collected from each stage by scraping and re-dispersed into water. Mass deposition was quantified using a fluorescent assay on BioTek Cytation 5 Multimode Imager. The assay utilized the inherent fluorescence of UiO-66 (excitation at 280 nm and emission at 390 nm) and a linear mass approximation.[25] From the deposition profiles on each plate, the mass median aerodynamic diameter, FPF, geometric standard deviation (GSD), ED and GSD were determined using particle size cutoffs for an NGI operating at 60 L/min.

***In Vitro* Cell Assays: Viability.** MH-S (ATCC CRL2019) murine alveolar macrophage and A549 (ATCC CCL185) human adenocarcinoma alveolar basal epithelial cell lines were cultured according to ATCC guidelines. All experiments were performed with cell lines not exceeding a passage number of ten. For *in vitro* cell viability assessment, MH-S and A549 cells were seeded in 96-well plates 24 h prior to treatment. Immediately prior to NP treatment, UiO-66 NPs were washed 3 times with DMF followed by three washes in sterile, endotoxin-free water and then resuspended in sterile RPMI or F-12 media (Gibco) supplemented with 10% fetal bovine serum (Gibco) and 1% penicillin−streptomycin (GE Healthcare HyClone) for MH-S and A549 cells, respectively. 4 and 24 h following treatment, cell viability was assessed using CellTiter-Glo 2.0 Cell Viability Assay (Promega) according to manufacturer's guidelines. Luminescence was recorded using BioTek Cytation 5 Multimode Imager and cell viability was calculated from luminescence data by normalizing to the untreated control.

***In Vitro* Cell Assays: Inflammation.** For *in vitro* assessment of inflammation, MH-S cells were seeded in 96-well plates 24 h prior to treatment. 4 and 24 h following treatment, 96-well plates were centrifuged at 1000 rpm for 10 min and the supernatants were collected and stored at −30 °C until inflammatory cytokine analysis. For cytokine analysis, enzyme-linked immunosorbent assays kits (BD Biosciences) for Interleukin-6 (IL-6) and TNF-α were performed on the supernatant according to manufacturer's guidelines.

***In Vitro* Cell Assays: Fluorescent Imaging.** UiO-66 NPs were loaded with FITC (Millipore Sigma) at an incubation ratio of 2:1 in DMF at 37 °C and 1000 rpm for 24 h. MH-S cells were seeded in an 8-chamber glass cover slip and allowed to adhere for 4 h before UiO-66 NP treatment. 24 h following treatment, cells were washed with PBS and fixed with 4% paraformaldehyde (PFA) (Alfa Aesar) in PBS for 15 min at room temperature. Cells were then permeabilized with 0.2% Triton-X solution in PBS for 10 min at room temperature. Phalloidin-TRITC stain (Millipore Sigma) was used to stain actin filaments at a 1:250 dilution in PBS for 20 min at room temperature. Nuclei were then stained with 700 nM DAPI for 10 min. To differentiate between internalization and surface binding of UiO-66 NPs, MH-S cells were treated with FITC-loaded NPs for 24 h and then washed once with PBS to remove free NPs. Trypan Blue dye (Gibco) was added at a final concentration of 2 mg/ml to quench any surface associated FITC signal. Imaging was performed using BioTek Cytation 5 Multimode Imager.

***In Vivo* Murine Inflammation Studies.** All studies involving animals were performed in accordance with National Institutes of Health (NIH) guidelines for the care and use of laboratory animals and approved by the Institutional Animal Care and Use Committee (IACUC) at the University of Delaware. C57BL/6J (Jackson Laboratories) were housed in a pathogen-free facility at the University of Delaware.

To assess airway inflammation, 50 μL volumes of UiO-66 NPs dispersions and controls in PBS were administered to 6−8 week-old female C57BL/6J mice *via* orotracheal instillation.[61,70] NPs/mouse (100 μg) as determined *via* TGA was administered and 0.2 μg LPS/mouse from *Escherichia coli* O111:B4 (Millipore Sigma) was administered as a positive control for airway inflammation. After 24 h following dosing, mice were euthanized and BAL was performed to collect BALF by cannulating the trachea and flushing the lungs with 3 sequential washes, 1 mL each, of PBS. The collected BALF was centrifuged and the supernatant was stored at −30 °C until inflammatory cytokine analysis. The cell pellet was washed twice with PBS supplemented with 2% fetal bovine serum and blocked with anti-CD16/32 (Fc block, BioLegend) for 10 min and then stained for 30 min with the following antibodies: CD45-FITC, Ly6G-APC, CD86-AlexaFluor700, I-A/I-E-Brilliant Violet 785 (all from BioLegend), and Siglec-F-APC-Cy7 (BD Biosciences). Cells were then fixed with 4% PFA for 15 min and then analyzed using ACEA NovoCyte Flow Cytometer for the isolation of alveolar macrophage and neutrophil populations. Median fluorescent intensity was recorded *via* flow cytometry as a measure of surface marker expression.

***In Vivo* Murine Biodistribution Studies.** To assess zirconium biodistribution, 6−8 week-old female C57BL/6J mice were dosed with 100 μg of UiO-66 NPs *via* orotracheal instillation with concentrations determined *via* TGA. At 1 and 7 day time points, mice were euthanized, blood was collected by cardiac puncture, and organs were harvested and weighed. Organs were then minced and digested for 24 h in trace metal grade nitric acid (2 mL for heart, lungs, kidneys, and spleen, 4 mL for liver, and 1 mL for blood, Fisher Scientific) at 75 °C. After the 24 h period, trace metal grade hydrochloric acid (Fisher Scientific) was added in the amount of 25% of the original volume of nitric acid (0.25, 0.5, or 1 mL). The resulting digested organs and blood were then filtered through a 0.22 μm filter, diluted to 4% nitric acid in DI water from a Milli-Q DI water system, and analyzed for their zirconium content *via* ICP−MS using an Agilent 7500 ICP−MS.

Histology. Tracheas were cannulated and filled with 4% PFA in PBS to fully inflate the lungs. The lungs were harvested and stored in 4% PFA. For histological analysis, the lungs were embedded in paraffin and cut at 7 μm sections. Sections were mounted to glass slides and stained using H&E. Stained sections were imaged using BioTek Cytation 5 Multimode Imager.

Statistics. GraphPad Prism 8 (GraphPad Software Inc) was used to perform statistical analysis. Figure captions denote the statistical tests used to carry out the analysis. All quantitative data are represented as mean ± standard deviation or standard error of the mean. Tukey's multiple comparisons test, Dunnett's multiple comparisons test, Sidak's multiple comparisons test, or Student's *T*-test were used to generate *p*-values unless stated otherwise.

■ ASSOCIATED CONTENT

Supporting Information

The Supporting Information is available free of charge at https://pubs.acs.org/doi/10.1021/acsami.0c10900.

TGA combustion analyses of UiO-66 NP defectiveness; BET Isotherm results; aerosol characterization; NGI aerosol deposition profiles; cell viability and inflamma-

https://dx.doi.org/10.1021/acsami.0c10900
ACS Appl. Mater. Interfaces 2020, 12, 38989−39004

tory cytokines at the 4 h timepoint; Trypan Blue quenching for NP internalization studies; and BALF flow cytometry sample gating (PDF)

AUTHOR INFORMATION

Corresponding Author

Catherine A. Fromen − *Department of Chemical and Biomolecular Engineering, University of Delaware, Newark, Delaware 19716, United States;* orcid.org/0000-0002-7528-0997; Phone: (302) 831-3649; Email: cfromen@udel.edu

Authors

Bader M. Jarai − *Department of Chemical and Biomolecular Engineering, University of Delaware, Newark, Delaware 19716, United States;* orcid.org/0000-0001-7099-2461

Zachary Stillman − *Department of Chemical and Biomolecular Engineering, University of Delaware, Newark, Delaware 19716, United States*

Lucas Attia − *Department of Chemical and Biomolecular Engineering, University of Delaware, Newark, Delaware 19716, United States;* orcid.org/0000-0002-9941-3846

Gerald E. Decker − *Department of Chemistry and Biochemistry, University of Delaware, Newark, Delaware 19716, United States*

Eric D. Bloch − *Department of Chemistry and Biochemistry, University of Delaware, Newark, Delaware 19716, United States;* orcid.org/0000-0003-4507-6247

Complete contact information is available at: https://pubs.acs.org/10.1021/acsami.0c10900

Author Contributions

[§]B.M.J. and Z.S. contributed equally.

Funding

Research reported in this publication was supported by the National Institutes of Health and the State of Delaware under award numbers P20GM104316 and P20GM103446, as well as a Research Starter Grant in Pharmaceutics from the PhRMA foundation; Z.S. was supported by a T32GM008550 training grant. The content is solely the responsibility of the authors and does not necessarily represent the official views of the National Institutes of Health.

Notes

The authors declare no competing financial interest.

ACKNOWLEDGMENTS

The authors acknowledge R. Locke and M. Killian for Histology assistance and C. Golt for ICP−MS assistance. Figures for abstract created with BioRender.com.

REFERENCES

(1) Zhao, M.; Yuan, K.; Wang, Y.; Li, G.; Guo, J.; Gu, L.; Hu, W.; Zhao, H.; Tang, Z. Metal−Organic Frameworks as Selectivity Regulators for Hydrogenation Reactions. *Nature* **2016**, *539*, 76−80.

(2) Trickett, C. A.; Helal, A.; Al-Maythalony, B. A.; Yamani, Z. H.; Cordova, K. E.; Yaghi, O. M. The Chemistry of Metal−Organic Frameworks for CO2 Capture, Regeneration and Conversion. *Nat. Rev. Mater.* **2017**, *2*, 17045.

(3) Wu, H.; Chua, Y. S.; Krungleviciute, V.; Tyagi, M.; Chen, P.; Yildirim, T.; Zhou, W. Unusual and Highly Tunable Missing-Linker Defects in Zirconium Metal-Organic Framework UiO-66 and Their Important Effects on Gas Adsorption. *J. Am. Chem. Soc.* **2013**, *135*, 10525−10532.

(4) Simon-Yarza, T.; Mielcarek, A.; Couvreur, P.; Serre, C. Nanoparticles of Metal-Organic Frameworks: On the Road to In Vivo Efficacy in Biomedicine. *Adv. Mater.* **2018**, *30*, 1707365.

(5) Lázaro, I. A.; Haddad, S.; Sacca, S.; Orellana-Tavra, C.; Fairen-Jimenez, D.; Forgan, R. S. Selective Surface PEGylation of UiO-66 Nanoparticles for Enhanced Stability, Cell Uptake, and PH-Responsive Drug Delivery. *Chem* **2017**, *2*, 561−578.

(6) Lázaro, I. A.; Forgan, R. S. Application of Zirconium MOFs in Drug Delivery and Biomedicine. *Coord. Chem. Rev.* **2019**, *380*, 230−259.

(7) Sajid, M. Toxicity of Nanoscale Metal Organic Frameworks: A Perspective. *Environ. Sci. Pollut. Res.* **2016**, *23*, 14805−14807.

(8) Imaz, I.; Rubio-Martínez, M.; García-Fernández, L.; García, F.; Ruiz-Molina, D.; Hernando, J.; Puntes, V.; Maspoch, D. Coordination Polymer Particles as Potential Drug Delivery Systems. *Chem. Commun.* **2010**, *46*, 4737−4739.

(9) Wuttke, S.; Zimpel, A.; Bein, T.; Braig, S.; Stoiber, K.; Vollmar, A.; Müller, D.; Haastert-Talini, K.; Schaeske, J.; Stiesch, M. Validating Metal-Organic Framework Nanoparticles for Their Nanosafety in Diverse Biomedical Applications. *Adv. Healthcare Mater.* **2017**, *6*, 1600818.

(10) Wagner, A.; Liu, Q.; Rose, O. L.; Eden, A.; Vijay, A.; Rojanasakul, Y.; Dinu, C. Z. Toxicity Screening of Two Prevalent Metal Organic Frameworks for Therapeutic Use in Human Lung Epithelial Cells. *Int. J. Nanomed.* **2019**, *14*, 7583−7591.

(11) DeCoste, J. B.; Peterson, G. W.; Jasuja, H.; Glover, T. G.; Huang, Y.-g.; Walton, K. S. Stability and Degradation Mechanisms of Metal-Organic Frameworks Containing the $Zr_6O_4(OH)_4$ Secondary Building Unit. *J. Mater. Chem. A* **2013**, *1*, 5642−5650.

(12) Orellana-Tavra, C.; Baxter, E. F.; Tian, T.; Bennett, T. D.; Slater, N. K. H.; Cheetham, A. K.; Fairen-Jimenez, D. Amorphous Metal-Organic Frameworks for Drug Delivery. *Chem. Commun.* **2015**, *51*, 13878.

(13) Shearer, G. C.; Chavan, S.; Ethiraj, J.; Vitillo, J. G.; Svelle, S.; Olsbye, U.; Lamberti, C.; Bordiga, S.; Lillerud, K. P. Tuned to Perfection: Ironing out the Defects in Metal-Organic Framework UiO-66. *Chem. Mater.* **2014**, *26*, 4068−4071.

(14) Cunha, D.; Ben Yahia, M.; Hall, S.; Miller, S. R.; Chevreau, H.; Elkaïm, E.; Maurin, G.; Horcajada, P.; Serre, C. Rationale of Drug Encapsulation and Release from Biocompatible Porous Metal−Organic Frameworks. *Chem. Mater.* **2013**, *25*, 2767−2776.

(15) Javanbakht, S.; Shadi, M.; Mohammadian, R.; Shaabani, A.; Amini, M. M.; Pooresmaeil, M.; Salehi, R. Facile Preparation of PH-Responsive k-Carrageenan/Tramadol Loaded UiO-66 Bio-Nanocomposite Hydrogel Beads as a Nontoxic Oral Delivery Vehicle. *J. Drug Deliv. Sci. Technol.* **2019**, *54*, 101311.

(16) Wyszogrodzka-Gaweł, G.; Dorożyński, P.; Giovagnoli, S.; Strzempek, W.; Pesta, E.; Węglarz, W. P.; Gil, B.; Menaszek, E.; Kulinowski, P. An Inhalable Theranostic System for Local Tuberculosis Treatment Containing an Isoniazid Loaded Metal Organic Framework Fe-MIL-101-NH2—From Raw MOF to Drug Delivery System. *Pharmaceutics* **2019**, *11*, 687.

(17) Hu, X.; Wang, C.; Wang, L.; Liu, Z.; Wu, L.; Zhang, G.; Yu, L.; Ren, X.; York, P.; Sun, L.; Zhang, J.; Li, H. Nanoporous CD-MOF Particles with Uniform and Inhalable Size for Pulmonary Delivery of Budesonide. *Int. J. Pharm.* **2019**, *564*, 153−161.

(18) Fernández-Paz, C.; Rojas, S.; Salcedo-Abraira, P.; Simón-Yarza, T.; Remuñán-López, C.; Horcajada, P. Metal−Organic Framework Microsphere Formulation for Pulmonary Administration. *ACS Appl. Mater. Interfaces* **2020**, *12*, 25676−25682.

(19) Labiris, N. R.; Dolovich, M. B. Pulmonary Drug Delivery. Part I: Physiological Factors Affecting Therapeutic Effectiveness of Aerosolized Medications. *Br. J. Clin. Pharmacol.* **2003**, *56*, 588−599.

(20) Roth, G. A.; Abate, D.; Abate, K. H.; Abay, S. M.; Abbafati, C.; Abbasi, N.; Abbastabar, H.; Abd-Allah, F.; Abdela, J.; Abdelalim, A. Global, Regional, and National Age-Sex-Specific Mortality for 282 Causes of Death in 195 Countries and Territories, 1980−2017: A Systematic Analysis for the Global Burden of Disease Study 2017. *Lancet* **2018**, *392*, 1736−1788.

(21) Vabret, N.; Britton, G. J.; Gruber, C.; Hegde, S.; Kim, J.; Kuksin, M.; Levantovsky, R.; Malle, L.; Moreira, A.; Park, M. D. Immunology of COVID-19: Current State of the Science. *Immunity* **2020**, *52*, 910.
(22) Patton, J. S.; Byron, P. R. Inhaling Medicines: Delivering Drugs to the Body through the Lungs. *Nat. Rev. Drug Discovery* **2007**, *6*, 67−74.
(23) Musante, C. J.; Schroeter, J. D.; Rosati, J. A.; Crowder, T. M.; Hickey, A. J.; Martonen, T. B. Factors Affecting the Deposition of Inhaled Porous Drug Particles. *J. Pharm. Sci.* **2002**, *91*, 1590−1600.
(24) Edwards, D. A.; Hanes, J.; Caponetti, G.; Hrkach, J.; Ben-Jebria, A.; Eskew, M. L.; Mintzes, J.; Deaver, D.; Lotan, N.; Langer, R. Large Porous Particles for Pulmonary Drug Delivery. *Science* **1997**, *276*, 1868−1872.
(25) Decker, G. E.; Stillman, Z.; Attia, L.; Fromen, C. A.; Bloch, E. D. Controlling Size, Defectiveness, and Fluorescence in Nanoparticle UiO-66 Through Water and Ligand Modulation. *Chem. Mater.* **2019**, *31*, 4831−4839.
(26) Wang, L.-J.; Li, J.; Hao, F.-R.; Yuan, Y.; Li, J.-Y.; Lu, W.; Zhou, T.-Y. Dexamethasone Suppresses the Growth of Human Non-Small Cell Lung Cancer via Inducing Estrogen Sulfotransferase and Inactivating Estrogen. *Acta Pharmacol. Sin.* **2016**, *37*, 845−856.
(27) Farne, H.; Kumar, K.; Ritchie, A. I.; Finney, L. J.; Johnston, S. L.; Singanayagam, A. Repurposing Existing Drugs for the Treatment of COVID-19. *Ann. Am. Thorac. Soc.* **2020**.
(28) Azhar, M. R.; Abid, H. R.; Periasamy, V.; Sun, H.; Tade, M. O.; Wang, S. Adsorptive Removal of Antibiotic Sulfonamide by UiO-66 and ZIF-67 for Wastewater Treatment. *J. Colloid Interface Sci.* **2017**, *500*, 88−95.
(29) He, C.; Hu, Y.; Yin, L.; Tang, C.; Yin, C. Effects of Particle Size and Surface Charge on Cellular Uptake and Biodistribution of Polymeric Nanoparticles. *Biomaterials* **2010**, *31*, 3657−3666.
(30) Schuster, B. S.; Suk, J. S.; Woodworth, G. F.; Hanes, J. Nanoparticle Diffusion in Respiratory Mucus from Humans without Lung Disease. *Biomaterials* **2013**, *34*, 3439−3446.
(31) Bleecker, E. R.; Menzies-Gow, A. N.; Price, D. B.; Bourdin, A.; Sweet, S.; Martin, A. L.; Alacqua, M.; Tran, T. N. Systematic Literature Review of Systemic Corticosteroid Use for Asthma Management. *Am. J. Respir. Crit. Care Med.* **2020**, *201*, 276−293.
(32) Sun, W.; Li, H.; Li, H.; Li, S.; Cao, X. Adsorption Mechanisms of Ibuprofen and Naproxen to UiO-66 and UiO-66-NH2: Batch Experiment and DFT Calculation. *Chem. Eng. J.* **2019**, *360*, 645−653.
(33) Wu, M.-X.; Yang, Y.-W. Metal−Organic Framework (MOF)-Based Drug/Cargo Delivery and Cancer Therapy. *Adv. Mater.* **2017**, *29*, 1606134.
(34) Jiao, Y.; Liu, Y.; Zhu, G.; Hungerford, J. T.; Bhattacharyya, S.; Lively, R. P.; Sholl, D. S.; Walton, K. S. Heat-Treatment of Defective UiO-66 from Modulated Synthesis: Adsorption and Stability Studies. *J. Phys. Chem. C* **2017**, *121*, 23471−23479.
(35) Wei, J.; Zhang, W.; Pan, W.; Li, C.; Sun, W. Experimental and Theoretical Investigations on Se(Iv) and Se(vi) Adsorption to UiO-66-Based Metal−Organic Frameworks. *Environ. Sci.: Nano* **2018**, *5*, 1441−1453.
(36) Pelfrêne, A.; Cave, M.; Wragg, J.; Douay, F. In Vitro Investigations of Human Bioaccessibility from Reference Materials Using Simulated Lung Fluids. *Int. J. Environ. Res. Publ. Health* **2017**, *14*, 112.
(37) Shinohara, N.; Zhang, G.; Oshima, Y.; Kobayashi, T.; Imatanaka, N.; Nakai, M.; Sasaki, T.; Kawaguchi, K.; Gamo, M. Kinetics and Dissolution of Intratracheally Administered Nickel Oxide Nanomaterials in Rats. *Part. Fibre Toxicol.* **2017**, *14*, 48.
(38) Calas, A.; Uzu, G.; Martins, J. M. F.; Voisin, D.; Spadini, L.; Lacroix, T.; Jaffrezo, J.-L. The Importance of Simulated Lung Fluid (SLF) Extractions for a More Relevant Evaluation of the Oxidative Potential of Particulate Matter. *Sci. Rep.* **2017**, *7*, 11617.
(39) Kato, Y.; Ozawa, S.; Miyamoto, C.; Maehata, Y.; Suzuki, A.; Maeda, T.; Baba, Y. Acidic Extracellular Microenvironment and Cancer. *Canc. Cell Int.* **2013**, *13*, 89.
(40) Bhardwaj, A.; Grobler, A.; Rath, G.; Kumar Goyal, A.; Kumar Jain, A.; Mehta, A. Pulmonary Delivery of Anti-Tubercular Drugs Using Ligand Anchored PH Sensitive Liposomes for the Treatment of Pulmonary Tuberculosis. *Curr. Drug Delivery* **2016**, *13*, 909−922.
(41) Xu, C.; Tian, H.; Sun, H.; Jiao, Z.; Zhang, Y.; Chen, X. A PH Sensitive Co-Delivery System of SiRNA and Doxorubicin for Pulmonary Administration to B16F10 Metastatic Lung Cancer. *RSC Adv.* **2015**, *5*, 103380−103385.
(42) Dong, H.; Yang, G. X.; Zhang, X.; Meng, X. B.; Sheng, J. L.; Sun, X. J.; Feng, Y. J.; Zhang, F. M. Folic Acid Functionalized Zirconium-Based Metal−Organic Frameworks as Drug Carriers for Active Tumor-Targeted Drug Delivery. *Chem.—Eur. J.* **2018**, *24*, 17148−17154.
(43) Nagata, S.; Kokado, K.; Sada, K. Metal-organic framework tethering PNIPAM for ON-OFF controlled release in solution. *Chem. Commun.* **2015**, *51*, 8614−8617.
(44) Sun, C.-Y.; Qin, C.; Wang, X.-L.; Yang, G.-S.; Shao, K.-Z.; Lan, Y.-Q.; Su, Z.-M.; Huang, P.; Wang, C.-G.; Wang, E.-B. Zeolitic Imidazolate Framework-8 as Efficient PH-Sensitive Drug Delivery Vehicle. *Dalton Trans.* **2012**, *41*, 6906−6909.
(45) Fromen, C. A.; Shen, T. W.; Larus, A. E.; Mack, P.; Maynor, B. W.; Luft, J. C.; DeSimone, J. M. Synthesis and Characterization of Monodisperse Uniformly Shaped Respirable Aerosols. *AIChE J.* **2013**, *59*, 3184−3194.
(46) Stone, R. C.; Johnson, D. L. A Note on the Effect of Nebulization Time and Pressure on the Culturability of Bacillus Subtilis and Pseudomonas Fluorescens. *Aerosol Sci. Technol.* **2002**, *36*, 536−539.
(47) Lavorini, F.; Pistolesi, M.; Usmani, O. S. Recent Advances in Capsule-Based Dry Powder Inhaler Technology. *Multidiscip. Respir. Med.* **2017**, *12*, 11.
(48) Garcia, A.; Mack, P.; Williams, S.; Fromen, C.; Shen, T.; Tully, J.; Pillai, J.; Kuehl, P.; Napier, M.; DeSimone, J. M. Microfabricated Engineered Particle Systems for Respiratory Drug Delivery and Other Pharmaceutical Applications. *J. Drug Deliv.* **2012**, *2012*, 941243.
(49) Gandara-Loe, J.; Ortuno-Lizarán, I.; Fernández-Sanchez, L.; Alió, J. L.; Cuenca, N.; Vega-Estrada, A.; Silvestre-Albero, J. Metal-Organic Frameworks as Drug Delivery Platforms for Ocular Therapeutics. *ACS Appl. Mater. Interfaces* **2019**, *11*, 1924.
(50) Su, F.; Jia, Q.; Li, Z.; Wang, M.; He, L.; Peng, D.; Song, Y.; Zhang, Z.; Fang, S. Aptamer-Templated Silver Nanoclusters Embedded in Zirconium Metal−Organic Framework for Targeted Antitumor Drug Delivery. *Microporous Mesoporous Mater.* **2019**, *275*, 152.
(51) Mohamed, N. A.; Davies, R. P.; Lickiss, P. D.; Ahmetaj-Shala, B.; Reed, D. M.; Gashaw, H. H.; Saleem, H.; Freeman, G. R.; George, P. M.; Wort, S. J. Chemical and Biological Assessment of Metal Organic Frameworks (MOFs) in Pulmonary Cells and in an Acute in Vivo Model: Relevance to Pulmonary Arterial Hypertension Therapy. *Pulm. Circ.* **2017**, *7*, 643.
(52) Jarai, B. M.; Kolewe, E. L.; Stillman, Z. S.; Raman, N.; Fromen, C. A. Polymeric Nanoparticles. *Nanoparticles for Biomedical Applications*; Elsevier, 2020; pp 303−324.
(53) Guo, A.; Durymanov, M.; Permyakova, A.; Sene, S.; Serre, C.; Reineke, J. Metal Organic Framework (MOF) Particles as Potential Bacteria-Mimicking Delivery Systems for Infectious Diseases: Characterization and Cellular Internalization in Alveolar Macrophages. *Pharm. Res.* **2019**, *36*, 53.
(54) Arcuri, C.; Monarca, L.; Ragonese, F.; Mecca, C.; Bruscoli, S.; Giovagnoli, S.; Donato, R.; Bereshchenko, O.; Fioretti, B.; Costantino, F. Probing Internalization Effects and Biocompatibility of Ultrasmall Zirconium Metal-Organic Frameworks UiO-66 NP in U251 Glioblastoma Cancer Cells. *Nanomaterials* **2018**, *8*, 867.
(55) Duan, F.; Feng, X.; Yang, X.; Sun, W.; Jin, Y.; Liu, H.; Ge, K.; Li, Z.; Zhang, J. A Simple and Powerful Co-Delivery System Based on PH-Responsive Metal-Organic Frameworks for Enhanced Cancer Immunotherapy. *Biomaterials* **2017**, *122*, 23.
(56) Blank, F.; Stumbles, P. A.; Seydoux, E.; Holt, P. G.; Fink, A.; Rothen-Rutishauser, B.; Strickland, D. H.; Von Garnier, C. Size-

Dependent Uptake of Particles by Pulmonary Antigen-Presenting Cell Populations and Trafficking to Regional Lymph Nodes. *Am. J. Respir. Cell Mol. Biol.* **2013**, *49*, 67.
(57) Shen, T. W.; Fromen, C. A.; Kai, M. P.; Luft, J. C.; Rahhal, T. B.; Robbins, G. R.; DeSimone, J. M. Distribution and Cellular Uptake of PEGylated Polymeric Particles in the Lung Towards Cell-Specific Targeted Delivery. *Pharm. Res.* **2015**, *32*, 3248−3260.
(58) Detampel, P.; Ganguly, A.; Tehranian, S.; Green, F.; Singha, S.; Santamaria, P.; Jeje, A. A.; Cho, C. S.; Petri, B.; Amrein, M. W. In Vivo Clearance of Nanoparticles by Transcytosis across Alveolar Epithelial Cells. *PLoS One* **2019**, *14*, No. e0223339.
(59) Fröhlich, E. The Role of Surface Charge in Cellular Uptake and Cytotoxicity of Medical Nanoparticles. *Int. J. Nanomed.* **2012**, *7*, 5577−5591.
(60) Guilliams, M.; Lambrecht, B. N.; Hammad, H. Division of Labor between Lung Dendritic Cells and Macrophages in the Defense against Pulmonary Infections. *Mucosal Immunol.* **2013**, *6*, 464−473.
(61) Fromen, C. A.; Rahhal, T. B.; Robbins, G. R.; Kai, M. P.; Shen, T. W.; Luft, J. C.; DeSimone, J. M. Nanoparticle Surface Charge Impacts Distribution, Uptake and Lymph Node Trafficking by Pulmonary Antigen-Presenting Cells. *Nanomed. Nanotechnol. Biol. Med.* **2016**, *12*, 677−687.
(62) Roberts, R. A.; Shen, T.; Allen, I. C.; Hasan, W.; DeSimone, J. M.; Ting, J. P. Y. Analysis of the Murine Immune Response to Pulmonary Delivery of Precisely Fabricated Nano- and Microscale Particles. *PLoS One* **2013**, *8*, No. e62115.
(63) Baati, T.; Njim, L.; Neffati, F.; Kerkeni, A.; Bouttemi, M.; Gref, R.; Najjar, M. F.; Zakhama, A.; Couvreur, P.; Serre, C. In Depth Analysis of the in Vivo Toxicity of Nanoparticles of Porous Iron(Iii) Metal−Organic Frameworks. *Chem. Sci.* **2013**, *4*, 1597.
(64) Paranjpe, M.; Müller-Goymann, C. Nanoparticle-Mediated Pulmonary Drug Delivery: A Review. *Int. J. Mol. Sci.* **2014**, *15*, 5852−5873.
(65) Videira, M. A.; Gano, L.; Santos, C.; Neves, M.; Almeida, A. J. Lymphatic Uptake of Lipid Nanoparticles Following Endotracheal Administration. *J. Microencapsul.* **2006**, *23*, 855−862.
(66) Ghosh, S.; Sharma, A.; Talukder, G. Zirconium. *Biol. Trace Elem. Res.* **1992**, *35*, 247−271.
(67) Barua, S.; Mitragotri, S. Challenges Associated with Penetration of Nanoparticles across Cell and Tissue Barriers: A Review of Current Status and Future Prospects. *Nano Today* **2014**, *9*, 223−243.
(68) Woods, A.; Patel, A.; Spina, D.; Riffo-Vasquez, Y.; Babin-Morgan, A.; de Rosales, R. T. M.; Sunassee, K.; Clark, S.; Collins, H.; Bruce, K.; Dailey, L. A.; Forbes, B. In Vivo Biocompatibility, Clearance, and Biodistribution of Albumin Vehicles for Pulmonary Drug Delivery. *J. Controlled Release* **2015**, *210*, 1−9.
(69) Stillman, Z.; Jarai, B. M.; Raman, N.; Patel, P.; Fromen, C. A. Degradation Profiles of Poly(Ethylene Glycol)Diacrylate (PEGDA)-Based Hydrogel Nanoparticles. *Polym. Chem.* **2020**, *11*, 568−580.
(70) Allen, I. C. The Utilization of Oropharyngeal Intratracheal PAMP Administration and Bronchoalveolar Lavage to Evaluate the Host Immune Response in Mice. *J. Visualized Exp.* **2014**, *80*, No. e51391.

https://dx.doi.org/10.1021/acsami.0c10900
ACS Appl. Mater. Interfaces 2020, 12, 38989−39004